This is the author's final, peer-reviewed manuscript as accepted for publication (AAM). The version presented here may differ from the published version, or version of record, available through the publisher's website. This version does not track changes, errata, or withdrawals on the publisher's site.

Co-crystals, salts, and ionic co-crystals of ethanol and ammonia

A. Dominic Fortes

Published version information

Citation: AD Fortes. "Co-crystals, salts and ionic co-crystals of ethanol and ammonia." ACS Earth and Space Chemistry (2020).

DOI: 10.1021/acsearthspacechem.0c00155

This document is the unedited author's version of a Submitted Work that was subsequently accepted for publication in ACS Earth and Space Chemistry, ©2020 American Chemical Society, after peer review. To access the final edited and published work see the DOI above.

Please cite only the published version using the reference above. This is the citation assigned by the publisher at the time of issuing the AAM. Please check the publisher's website for any updates.

This item was retrieved from **ePubs**, the Open Access archive of the Science and Technology Facilities Council, UK. Please contact epubs@stfc.ac.uk or go to http://epubs.stfc.ac.uk/ for further information and policies.

Co-crystals, Salts and Ionic Co-crystals of Ethanol and Ammonia

A. Dominic Fortes,[1,2,*]

[1] ISIS Neutron & Muon Spallation Source, Rutherford Appleton Laboratory, Harwell Science and Innovation Campus, Chilton, Oxfordshire, OX11 0QX, United Kingdom.

[2] Department of Earth Sciences, University College London, Gower Street, London WC1E 6BT, United Kingdom.

*Corresponding author email: dominic.fortes@stfc.ac.uk

Abstract

Compounds of ethanol and ammonia have been known for over a century but no structural characterisation has been carried out. Solid crystalline specimens of molecular ethanol mono-ammoniate and ethanol hemi-ammoniate were prepared by flash freezing of stoichiometric liquids in liquid nitrogen followed by annealing between 175 K and 195 K. High-resolution neutron powder diffraction measurements were used to determine the complete structures of the two compounds. Both are triclinic ($P\bar{1}$, Z = 2): ethanol mono-ammoniate is characterised by linear tapes of four-sided hydrogen-bonded rings, which extend along the crystal's *b*-axis; ethanol hemi-ammoniate's structure is defined by sheets (in the crystal's $a - b$ plane) comprised of two different types of four- and six-sided H-bonded rings. Measurements collected as a function of temperature provide a precise determination of the thermal expansion of the two ethanol ammoniates and of solid deutero-ammonia. Density Functional Theory calculations yield insights into the response of each structure to hydrostatic stress, including a proton transfer to form either wholly ionic ammonium ethoxide crystals or ionic co-crystals of ethanol ammonium ethoxide. The switch from molecular to ionic co-crystal in ethanol hemi-ammoniate may occur on cooling at ambient pressure, with kinetic frustration due to the low temperature of the transition.

Proton transfer at ambient pressure, or at modest impact shock pressures, suggests that there may be extensive ammonium salt formation amongst compounds of the simplest alcohols. This may

represent an important additional mechanism for the generation of NH_4^+ spectroscopic signatures in remotely sensed data from interstellar, cometary and planetary ices.

Keywords: ethanol, ammonia, co-crystal, neutron diffraction, hydrogen bonds, proton transfer, DFT

Introduction

Compounds of alcohols with simple molecules such as water and/or ammonia provide fertile ground for evaluating the competing effects of hydrogen-bond strength on crystal structures and properties.[1,2] They contain a range of moderately strong O–H···O hydrogen bonds through to weak C–H···O hydrogen bonds. The balance of these interactions may have striking consequences for the overall bulk behaviour, including phenomena such as negative linear compressibility.[3]

Furthermore, these molecules are cosmically abundant; methanol, ethanol and possibly heavier alcohols, form a significant fraction of the mantles of ice grains in star-forming regions,[4,5] being the most abundant complex organic molecules known in space.[6] Similarly, ammonia is an abundant component of interstellar ices.[7,8] These molecules inevitably find their way into the building blocks of planetary systems, the residue of which in our own solar system is a reservoir of comets. Methanol, ethanol, ethylene glycol and even glycoaldehyde have been detected in cometary ices[9] along with more prevalent water and ammonia.[10,11] Alternatively, organic molecules such as ethanol, urea and acetic acid may result from hydrothermal processing of molten ices through the rocky cores of icy planetary bodies[12] that we know to be rich in water and ammonia ices.[13,14] Consequently, there may be widespread opportunities for simple alcohol hydrates and ammoniates to form in space, on the surfaces or in the interiors of planetary objects.[15] There is therefore both an intellectual and a practical interest in characterising the structures and physical properties of these compounds.

The solid-liquid equilibria (SLE) in the ethanol–ammonia binary system at atmospheric pressure were reported by Broderson,[16] from which the existence of several compounds was inferred (Figure 1). These include ethanol hemi- and mono-ammoniates as well as an ammonia-rich solid that Broderson determined to be a solid-solution. No evidence of similar solid-solutions is found in any other mixtures of ammonia with small alcohol molecules[15,17,18] so Broderson's measurements of the ethanol-ammonia binary system, if correct, may have far-reaching implications.

This objective of this work, which forms part of wider study into the crystallography of simple alcohol – ammonia co-crystals,[19-21] was to confirm the existence of Broderson's proposed ethanol ammoniates, to determine their crystal structures and both measure and compute various physical properties. Variable-temperature neutron powder-diffraction was the method of choice in carrying

out the work since it allows for straightforward *in situ* studies of phase behaviour whilst also providing data required for phase identification and structure solution, including the positions and displacement parameters of the hydrogen atoms. This is particularly important since hydrogen bonds are expected to be the defining structural elements of these types of materials.

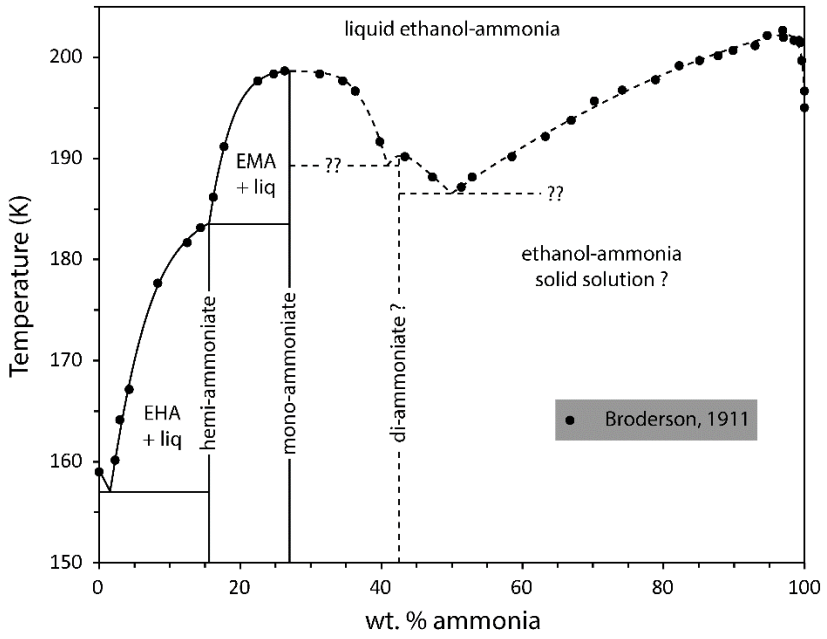

Figure 1

Ethanol-ammonia binary phase diagram at 1 bar after Broderson.[16] Dashed lines and the hypothetical ethanol di-ammoniate compound reflect a possible interpretation of the kink in the liquidus curve data around 40 wt. % NH_3. The three compositions examined as part of this work are denoted by the vertical solid and dashed lines labelled as hemi-, mono- and di-ammoniate.

Methods

Experimental methods

An evacuated glass bulb immersed in a dry-ice-cooled acetone bath (~220 K) was used to condense liquid deutero-ammonia (Sigma-Aldrich 422975, 99 atom % D). The condensed ammonia was divided into aliquots that were frozen, weighed and then mixed with appropriate quantities of perdeuterated ethanol (Sigma-Aldrich 186414, 99.5 atom % D) to form a series of

stoichiometric solutions. Liquids with three different compositions were prepared: 16.1 wt. % ND_3 in ethanol-d_6 (ethanol hemi-ammoniate, EHA), 27.8 wt. % ND_3 (ethanol mono-ammoniate, EMA) and 43.5 wt. % ND_3 (ethanol di-ammoniate, EDA). The purpose of the third sample was two-fold: firstly, it allows us to determine if the kink in Broderson's observed liquidus curves[16] can be explained by the existence of an ethanol di-ammoniate phase; secondly, if no di-ammoniate exists, it allows us to determine if another more ammonia-rich phase exists in the compositional space between EMA and solid ammonia, which may or may not be the proposed solid solution.

The liquid samples were flash frozen by direct immersion in liquid nitrogen. The transparent glassy solids were ground to a fine powder under liquid nitrogen and then transferred into a nitrogen-cooled slab-geometry sample holder composed of 6082-T6 Al-alloy with internal dimensions of 18 x 23 mm perpendicular to the beam, and 10 mm depth parallel to the incident beam. Once filled, the 'back' vanadium foil window of the sample can was attached with screws. Both the 'front' (i.e., beam-facing) and 'back' windows were sealed with 1 mm indium wire to prevent leakage of material from the interior. The front windows and the body of the sample holder were masked with Gd and Cd foil.

Time-of-flight neutron powder diffraction data were collected using the High Resolution Powder Diffractometer (HRPD) at the ISIS Neutron & Muon Spallation Source (Rutherford Appleton Laboratory, UK).[22] The bulk of the data collection was done in a neutron time-of-flight (TOF) 'window' between 100 and 200 milliseconds since this places Bragg peaks corresponding with *d*-spacings between 2.2 and 4.0 Å in the instrument's highest-resolution backscattering backs (average $2\theta = 168.33°$); for hydrogen-bonded molecular 'ices' this tends to be a region where the most intense peaks occur and the separation of lower-order peaks makes indexing of unknown powder patterns quite straightforward. For structure solution and refinement a number of datasets were also measured with the instrument's choppers phased to measure a 30 – 130 ms time-of-flight window, which captures Bragg peaks between 0.65 and 2.65 Å in the backscattering detectors.

Low temperatures were produced by means of a closed-cycle refrigerator (CCR), equipped with a Sumitomo Heavy Industries Ltd., RDK-415D2 cryo-cooler, mounted in the instrument's sample tank. The normal protocol was to maintain the temperature of the CCR cold head 30 – 40 K below the sample temperature whilst using a Watlow Firerod C1E-192 cartridge heater inserted into the frame of the sample holder itself to actively heat and control the sample temperature. The

sample temperature was measured using a RhFe resistance thermometer (fully-calibrated to ITS-1990), also inserted into the body of the sample holder.

All data underwent initial processing using the *Mantid* suite of powder-diffraction routines,[23] focussing data in each detector bank to a common scattering angle and then using a V:Nb null-scattering standard material to normalise with respect to the spectrum of the incident beam and correct for instrumental efficiency. The output data, in the form of logarithmically-binned histograms, were then analysed by the Rietveld[24] and LeBail[25] whole-pattern fitting methods using *GSAS*/*Expgui*.[26,27]

Initial examination of the first ethanol mono-ammoniate sample revealed that it was very poorly crystalline, exhibiting weak and broad Bragg peaks. On warming to 180 K, these sharpened and increased substantially in intensity. A structural dataset was obtained in the 30–130 ms and 100–200 ms time-of-flight windows (counted for 200 μA each).[a] Unfortunately, it was found that part of the gadolinium mask had broken during insertion into the CCR, resulting in the presence of some weak parasitic peaks from aluminium and steel in the diffraction pattern. The sample was recovered under liquid nitrogen and reloaded into another can with an intact Gd mask. This resulted in a slight loss of volatile ammonia and the re-quenched specimen was subsequently found to contain weak accessory peaks from what was later identified as ethanol hemi-ammoniate, EHA. Upon warming from 160 to 180 K, however, the EHA peaks disappeared (most likely because of partial melting) and it was possible to obtain a high-quality structural dataset from phase-pure EMA in the 30–130 ms and 100–200 ms time-of-flight windows counting for 200 and 120 μA, respectively. Re-cooling led to the reappearance of parasitic EHA peaks between 170 and 160 K.

The quenched EHA composition also required substantial annealing after mounting in the CCR to produce a satisfactory diffraction pattern. Since the peritectic melting point is lower for this composition, caution dictated that warming was stopped at 175 K and a structural dataset was collected in the 30–130 and 100–200 ms time-of-flight windows (200 μA each). Very small peaks attributable to EMA were identified in these data, indicating that the composition was slightly ammonia-rich. Data were collected on cooling to ~ 70 K in the 100–200 ms tof window, but there was such a considerable line broadening as the temperature was reduced (Suppl. Fig. S1) that

[a] The numbers are integrated proton beam currents, given as a proxy from the measurement duration. HRPD typically measures at a rate of 40 μA hr^{-1}, although this depends on a variety of factors, such as synchrotron trips and other losses. Hence the integrated beam current is a more meaningful indication of duration than the real-time length.

continuing further was considered not to be worthwhile. In light of the computational results detailed below, this decision might be construed as being premature.

After quenching and annealing of the di-ammoniate composition at 180 K it became apparent that the sample consisted of EMA and solid ammonia rather than a distinct crystalline phase of ethanol di-ammoniate or some component of a solid-solution. Profile refinement (see below) indicated that the mixture was 91(1) wt. % EMA and 9(1) wt. % solid ammonia. Assuming that the initial stoichiometry was accurate, the phase mixture should be ~ 78:22 rather than 91:9, which suggests that there is another non-crystalline ammonia-rich component present in the mixture. It is possible that not all of the originally glassy material devitrified at 180 K; perhaps additional crystallisation would have occurred on further warming. A structural dataset was collected in the 30–130 and 100–200 ms time-of-flight windows at 180 K (200 μA each), after which data were collected from the phase mixture on cooling to 10 K in steps of 10 K (counting for 20 μA each) and whilst there was a degree of line broadening it was not very severe. These data were therefore used to determine the thermal expansion of EMA and solid deutero-ammonia to high precision.

Computational method

Variable-pressure athermal geometry optimizations of the EHA and EMA structures were done using Density Functional Theory (DFT) and the plane-wave pseudopotential method[28,29] in order to evaluate details of the intra- and intermolecular geometry, the topology of the electron density and the effect of hydrostatic stress. The calculations were implemented in CASTEP[30-32] version 17.2 in conjunction with the analysis tools in the Materials Studio software package. Ultrasoft pseudopotentials with basis-set cut-offs of 1200 eV and $\vec{k}$-point grids with reciprocal lattice spacings of ~ 0.04 $Å^{-1}$ (6×5×3 for EMA and 5×4×3 for EHA) were required to achieve convergence of better than $1x10^{-2}$ GPa in the stress and better than $1x10^{-3}$ eV per atom in total energy. The 'PBE' gradient-corrected functional[33-34] was used in conjunction with the Tkatchenko & Scheffler (TS) dispersion correction[35] as this was found to provide accurate results in similar systems.[36] Structural relaxations were begun from the experimentally-obtained crystal structure using the BFGS method.[37] These were considered to have converged when the forces on each atom were less than $5x10^{-3}$ eV $Å^{-1}$ and each component of the stress tensor was smaller than 0.005 GPa.

Post-processing of the DFT calculations was done using C2X,[38] Vesta[39] and AIM-UC.[40]

Results

Indexing of the diffraction patterns

Unlike the two known *methanol* ammoniates, which are orthorhombic,[19,20] both of the ethanol ammoniates are triclinic.

The 180 K powder diffraction data from EMA were indexed using DICVOL06[41] with a reduced triclinic cell of dimensions a = 4.0695 Å, b = 5.1759 Å, c = 10.3822 Å, α = 94.861°, β = 94.922°, γ = 97.643°. The figures of merit[42,43] were M(21) = 60.1 and F(21) = 94.0 [0.0060, 37]. Using the molecular volumes of C_2H_5OH and ND_3 in their ambient-pressure crystalline phases,[44,45] we can obtain an estimate of the unit-cell volume as a function of the number of formula units per unit-cell. The case of Z = 2 yields V = 216.585 Å^3, which differs from the indexed unit-cell volume (214.92 Å^3) by only 0.8 %.

The 175 K powder diffraction data from EHA were similarly indexed with a reduced triclinic cell of dimensions a = 5.4900 Å, b = 7.1120 Å, c = 10.0618 Å, α = 104.389°, β = 100.232°, γ = 96.153°. The figures of merit[42,43] were M(15) = 75.1 and F(15) = 120.1 [0.0045, 28]. As with EMA, the unit-cell volume, 369.74 Å, differs by only ~ 1 % from the expected value for Z = 2 and a 2:1 ratio of ethanol to ammonia using the molecular volumes from the pure crystalline phases.

Structure solution and refinement

The crystal structures of EMA and EHA were each solved in space-group $P\bar{1}$ using the parallel tempering algorithm implemented in FOX,[46,47] version 1.6.99. Molecules in the form of Z-matrices were placed randomly in the asymmetric unit and the structure was then optimized against the powder diffraction data over twenty-five runs of 10 million trials. Whilst the ammonia molecules were kept rigid during this process, the ethanol molecules were permitted sufficient flexibility to allow either *trans* or *gauche* conformations to occur. The optimizations consistently produced very similar structures with chemically sensible molecular arrangements. The structure with the lowest overall cost function was exported as a CIF file to form the basis for Rietveld refinement with GSAS.

Structure refinements of both ammoniates were done using HRPD backscattering data measured in both the 30–130 and 100–200 ms time-of-flight windows. Due to the high homologous temperature and the resulting intensity decay to short times, the data below 40 ms were excluded; one additional artefact just below 60 ms was also excluded. The resulting model fits are shown in Figure 2 (EMA) and Figure 3 (EHA).

A model of the EMA structure with fully anisotropic atomic displacement parameters (ADPs) yielded wR_P = 1.90 % for all 5764 data points and χ^2 = 2.157 for 119 variables. The refinement required inclusion of an absorption parameter and a small degree of preferred orientation (2nd order spherical-harmonic model with a texture index of 1.013).

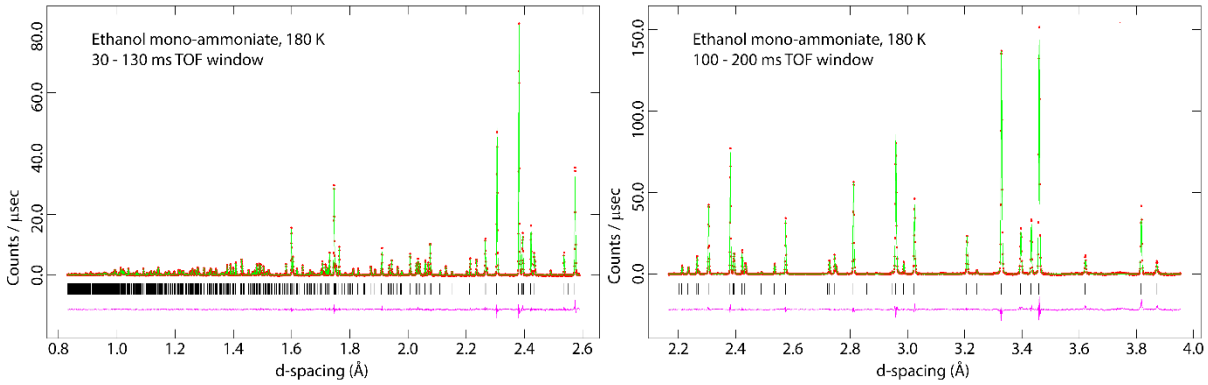

Figure 2

Background-subtracted neutron powder diffraction pattern of ethanol mono-ammoniate collected at 180 K in HRPD's 30–130 ms time-of flight window (left) and the 100–200 ms TOF window (right). Filled red circles show the measured intensities, the green line is a Rietveld model fit and the purple trace underneath the diffraction pattern is the difference profile. Black vertical tick marks show the expected positions of Bragg peaks.

The EHA model structure was similarly refined anisotropically to give wR_P = 1.57 % for all 5815 data points and χ^2 = 2.459 for 231 variables. The refinement also required inclusion of an absorption parameter and a small degree of preferred orientation (2nd order spherical-harmonic model with a texture index of 1.019). The structure refinement of EHA reported here was done without EMA being included as an accessory phase. EMA was determined to be present at the level of 1.05(4) wt. % and the only discernible peaks were in the 100–200 ms time-of-flight

window, where they were very small and well separated from the peaks of EHA. Refinements done with and without EMA yielded no significant difference in the structural model of EHA, including the ADPs, that was obtained.

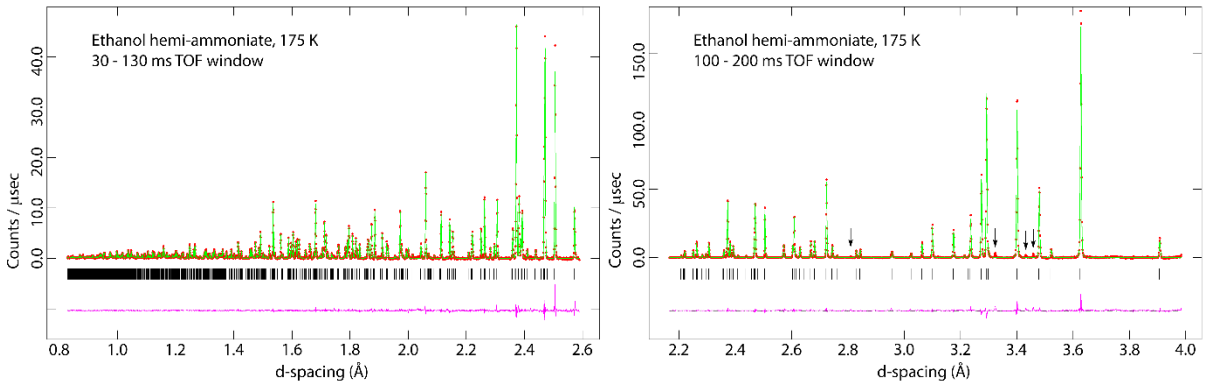

Figure 3

Background-subtracted neutron powder diffraction pattern of ethanol hemi-ammoniate collected at 175 K in HRPD's 30–130 ms time-of flight window (left) and the 100–200 ms TOF window (right). Symbols and lines have the same meaning as in Figure 2. Arrows indicate the only visible peaks from EMA in this dataset.

Structures of the ethanol – ammonia co-crystals

Table 1 reports the internal geometry of the ethanol-d_6 molecules in both ammoniates compared with the DFT calculations. Atomic coordinates, ADPs (U_{ij}), equivalent isotropic displacement parameters (U_{iso}) and complete tables of bond lengths and angles are provided in Supplementary CIFs. In the *Pc* form of solid ethanol,[44] one encounters both *trans* and *gauche*$^-$ conformers of the molecule. Since the asymmetric unit of EMA contains only a single ethanol molecule there can clearly be only one conformer, which is *trans*. However, in EHA, the ethanol molecule that donates a hydrogen bond to its neighbouring ethanol is *gauche*$^-$ and the ethanol molecule that donates a hydrogen bond to ammonia is *trans*. In all instances, the conformation about the C–C backbone is staggered. The DFT calculations produce quite similar C–C and C–O distances in the ethanol molecules of EMA and both conformations of ethanol in EHA. However, the experimental data

for the *gauche*$^{-}$ ethanol molecule in EHA differ significantly from the *trans* molecule; further data is required to understand the nature and origin of this apparent difference.

Table 1

Internal geometry of the ethanol molecules in the two ammoniates from the finite-temperature experimental data and from the athermal DFT calculations.

Ethanol hemi-ammoniate						Ethanol mono-ammoniate		
Gauche^{-} molecule	Expt.	DFT	*Trans* molecule	Expt.	DFT	*Trans* molecule	Expt.	DFT
C1–C2	1.466(8)	1.5163	C3–C4	1.486(7)	1.5120	C1–C2	1.490(5)	1.5117
C2–O1	1.442(8)	1.4385	C4–O2	1.405(6)	1.4361	C2–O1	1.411(4)	1.4276
C1–D4	1.092(8)	1.0978	C3–D10	1.069(11)	1.0973	C1–D4	1.060(5)	1.0975
C1–D5	1.052(9)	1.0984	C3–D11	1.080(13)	1.0983	C1–D5	1.067(6)	1.0967
C1–D6	1.066(10)	1.0965	C3–D12	1.080(7)	1.0968	C1–D6	1.084(5)	1.0964
C2–D7	1.041(8)	1.0999	C4–D13	1.059(7)	1.1021	C2–D7	1.099(4)	1.1050
C2–D8	1.067(8)	1.1023	C4–D14	1.077(8)	1.1028	C2–D8	1.080(5)	1.1049
O1–D9	0.977(7)	1.0182	O1–D15	1.001(7)	1.0425	O1–D9	1.008(4)	1.0317
D4–C1–D5	108.0(7)	107.700	D10–C3–D11	108.2(10)	107.951	D4–C1–D5	107.2(4)	108.025
D4–C1–D6	106.7(7)	107.969	D10–C3–D12	112.8(7)	108.591	D4–C1–D6	107.8(4)	107.819
D5–C1–D6	111.5(8)	108.487	D11–C3–D12	108.2(7)	107.816	D5–C1–D6	108.4(5)	108.527
D7–C2–D8	104.2(7)	107.036	D13–C4–D14	102.9(6)	106.695	D7–C2–D8	107.8(4)	106.885
D9–O1–C2	107.3(5)	108.604	D15–O2–C4	107.6(5)	108.177	D9–O1–C2	108.7(3)	108.937
C1–C2–O1–D9	−101.2(6)	−101.105	C3–C4–O2–D15	153.9(5)	154.675	C1–C2–O1–D9	170.6(3)	170.296

The asymmetric units of the two co-crystals are shown in Figure 4 and Figure 5. As the measurements on both solids were carried out at high homologous temperatures, the displacement ellipsoids are inevitably very large.

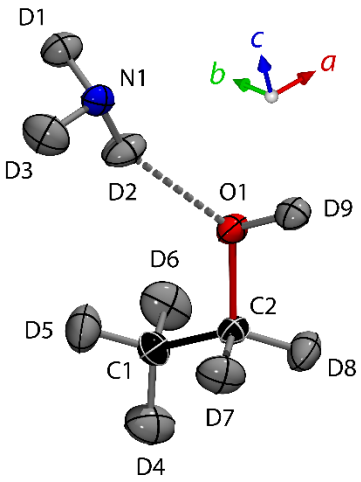

Figure 4

Asymmetric unit of ethanol mono-ammoniate, indicating the atom labelling scheme used throughout this work. Displacement ellipsoids, due to the high homologous temperature of the measurement and the resultant substantial thermal motion, are drawn at the 25 % probability level

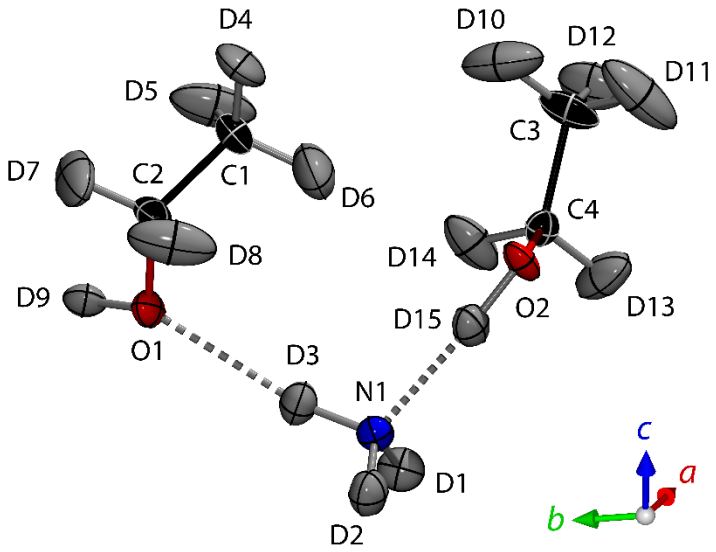

Figure 5

Asymmetric unit of ethanol hemi-ammoniate, indicating the atom labelling scheme used throughout this work. As in Figure 4, the displacement ellipsoids are drawn at the 25 % probability level.

The arrangement of molecules about inversion centres in EMA leads to the formation of two types of 4-sided hydrogen bonded rings (Figure 6), described in graph-set notation[48] as $R_4^4(8)$ and $R_2^2(8)$. Nearly identical $R_2^2(8)$ rings are found in the structure of methanol mono-ammoniate.[19] Both of the 4-sided rings share a common edge and extend as a corrugated tape along the *b*-axis of the crystal. No hydrogen bonding occurs between tapes packed along the *c*-axis; there are no plausible C–H···O or C–H···N contacts in the crystal at all, and the interactions are of a purely

van der Waals nature. Packing of the tapes along the *a*-axis is more interesting; the D3 deuterons of the ammonia molecule point alternately 'up' and 'down' along the *a*-axis at opposing corners of the four-sided rings. The contact to ammonia in the adjacent tapes is thus quite linear (N–D3···N ≈ 168°) but very long (N···N ≈ 4.07 Å), so could not reasonably described as a weak hydrogen bond, despite the obvious linearity. The ethanol O1 atoms in the adjacent tapes are slightly closer (N···O ≈ 3.63 Å) but the contact is very far from linear (N–D3···O1 ≈ 135°) although it should be noted that similar departures from H-bond linearity occur in solid ammonia.[45] The D···O distance remains substantially longer than the van der Waals radii sum (2.64 Å)[49] so this contact also cannot be categorised as a hydrogen bond. Geometric parameters of the hydrogen bonds in EMA are given in Table 2.

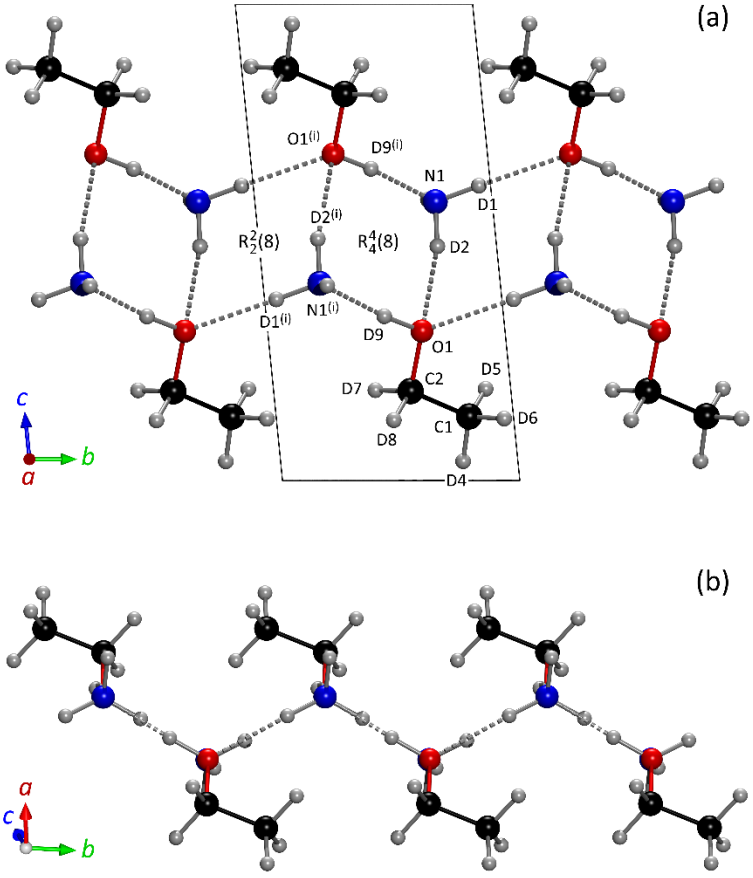

Figure 6

(a) Illustration of the hydrogen bonding network in ethanol mono-ammoniate, arranged into tapes of edge-sharing 4-sided rings along the *b*-axis. (b) The corrugation of these tapes, viewed along the N···O 'creases'. Symmetry codes: (i) 2−*x*, 1−*y*, 1−*z*.

Table 2

Experimentally-determined geometry of the hydrogen bonds in ethanol mono-ammoniate.

	D–H (Å)	H···A (Å)	D···A (Å)	D–H···A (°)
O1–D9···N1$^{(i)}$	1.008(4)	1.796(4)	2.801(4)	175.1(3)
N1–D1···O1$^{(ii)}$	1.005(4)	2.169(4)	3.170(4)	174.6(3)
N1–D2···O1	1.001(4)	2.198(5)	3.150(4)	158.5(3)
N1–D3···O1$^{(iii)}$	1.007(5)	2.844(5)	3.629(4)	135.3(3)

(i) 2−*x*, 1−*y*, 1−*z*: (ii) 2−*x*, 2−*y*, 1−*z*: (iii) 1−*x*, 1−*y*, 1−*z*.

Analysis of the electron density from DFT calculations provides some insight into the very long and weak inter-layer contacts. Figure 7 depicts a section of the electron density containing the long D3···O1 and D3···N1 contacts. Clearly, there is both a greater electron density, as well as a topological saddle point, along the D3···O1 vector. Whilst evidence has been presented that such features are not necessarily indicative of a chemical bond[50,51] and that the use of terms such 'bond critical points' is unwarranted,[52] the excellent summary of this debate by Taylor[53] does allow us to propose that the stronger of the two interactions is likely to be the most competitive. Hence it should not be surprising that the weak D3···O1 interaction is a particularly relevant aspect of the structure's response to both temperature and pressure, as detailed the sections below.

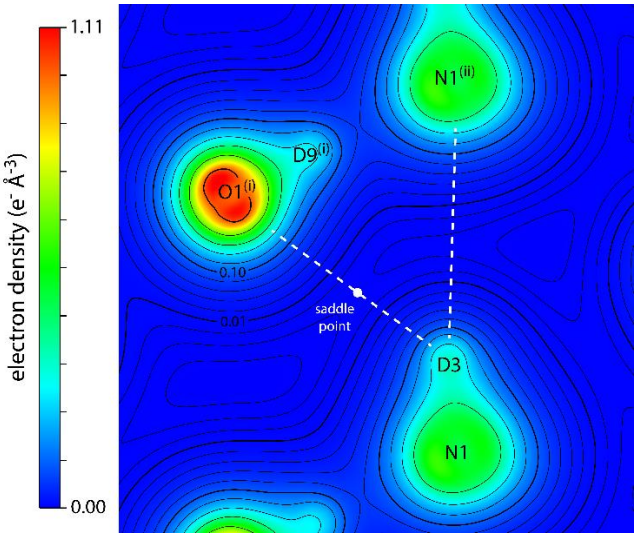

Figure 7

DFT-calculated electron density in a place defined by D3, O1$^{(i)}$ and N1$^{(ii)}$ revealing the presence of a saddle point between D3 and O1$^{(i)}$. The dashed white line between D3 and O1 represents the

interaction which develops into a full hydrogen bond under compression (Figure 13a). N.B. Contour lines are in logarithmic intervals. Symmetry codes: (i) 1−*x*, 1−*y*, 1−*z*; (ii) *x*−1, *y*, *z*.

The structure of EHA contains similar motifs to EMA, built around inversion centres. The same $R_2^2(8)$ rings occur, but the adjoining rings have the second ethanol molecule inserted so as to convert them from four-sided $R_4^4(8)$ rings into six-sided $R_6^6(12)$ rings (Figure 8). These extend as infinite tapes along the *b*-axis of the crystal. In EHA, however, there is further hydrogen bonding along the *a*-axis to form a second $R_2^2(8)$ ring (involving D2 and D3 instead of D1 and D3) and a second $R_6^6(12)$ ring (Figure 9). The two hexagonal rings differ in their geometry, one adopting a chair conformation and the other being planar. This network of 4- and 6-sided rings forms an infinite sheet in the *a*–*b* plane. There are two plausible candidate C–H···O hydrogen bonds, based on the literature definitions of length,[54] linearity[55] and electron density[56] for such interactions linking ethanol molecules within each sheet (Table 3). No hydrogen bonding occurs between the layers and, as in EMA, I conclude that the interactions along *c* are purely dispersive.

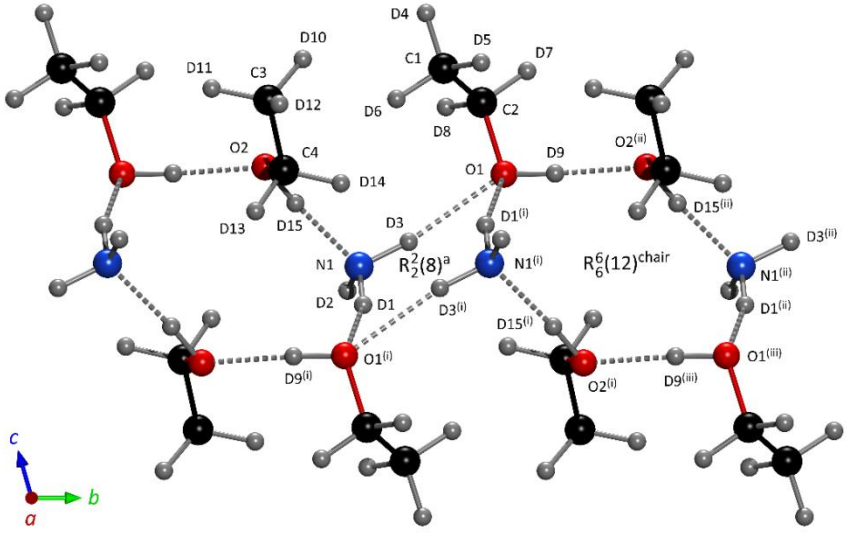

Figure 8

Illustration of part of the hydrogen bonding network in ethanol hemi-ammoniate showing the arrangement of $(C–H)_n$ groups about the sheet of 4- and 6-sided rings. Symmetry codes: (i) 1−*x*, 1−*y*, −*z*; (ii) *x*, 1+*y*, *z*; (iii) 1−*x*, 2−*y*, −*z*.

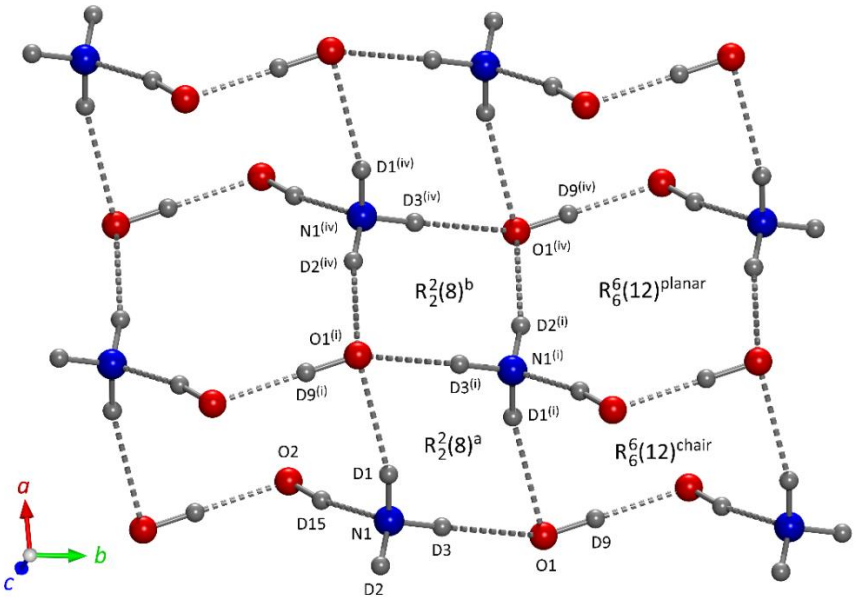

Figure 9

Wider view of the hydrogen bonding network in ethanol hemi-ammoniate with the $(C–H)_n$ groups omitted for clarity. Symmetry codes: (i) 1−*x*, 1−*y*, −z; (iv) 1+*x*, *y*, *z*.

Table 3

Experimentally-determined geometry of the hydrogen bonds in ethanol hemi-ammoniate.

	D–H (Å)	H···A (Å)	D···A (Å)	D–H···A (°)
O1–D9···O2$^{(i)}$	0.979(7)	1.747(7)	2.725(7)	177.5(6)
N–D1···O1$^{(ii)}$	1.011(6)	2.294(7)	3.239(6)	155.0(4)
N–D2···O1$^{(iii)}$	0.997(5)	2.203(6)	3.184(5)	167.9(5)
N–D3···O1	1.020(6)	2.177(6)	3.184(6)	169.1(5)
O2–D15···N	0.997(7)	1.785(7)	2.775(7)	171.7(5)
C1–D6···.O2	1.069(10)	2.783(9)	3.844(7)	171.8(7)
C3–D12···O2$^{(iv)}$	1.086(7)	2.659(7)	3.661(7)	153.3(4)

(i) *x*, 1+*y*, *z*: (ii) 1−*x*, 1−*y*, −*z*: (iii) −*x*, 1−*y*, −*z*: (iv) 1+*x*, *y*, *z*.

Thermal expansion of the ethanol – ammonia co-crystals

The unit-cell parameters of EMA as a function of temperature (10 – 180 K) are given in Suppl. Table S1 and plotted in Suppl. Fig. S2. Those of EHA (70 – 175 K) are provided in Suppl. Table S2 and Suppl. Fig. S3. In both compounds, precision at low temperatures is poorer due to broadening of the Bragg peaks, although the effect is more pronounced in the hemi-ammoniate.

In order to interpolate smoothly between these data and obtain some insight into the underlying vibrational characteristics of the material, the lattice parameters of EMA have been fitted with a second-order Grüneisen approximation to the zero-pressure equation of state (Eq. 1). In this approximation, the thermal expansion is considered equivalent to elastic strain such that,

$$V(T) = V_0 \left[1 + \frac{E(T)}{Q - bE(T)}\right] \qquad (1)$$

where V_0 is the unit cell volume at zero pressure, b = ½ (K_0'−1) and Q = ($V_0 K_0/\gamma$); K_0 is the zero pressure isothermal bulk modulus, K_0' is its first derivative with respect to pressure, and γ is the thermal Grüneisen parameter. The internal energy due to lattice vibrations, $E(T)$, is then determined via a Debye model:

$$E(T) = \frac{9nk_BT}{(\theta_D/T)^3} \int_0^{\theta_D/T} \frac{x^3}{e^x - 1} dx \qquad (2)$$

where θ_D is the Debye temperature, n is the number of atoms per formula unit, and k_B is the Boltzmann constant; the integral term is evaluated numerically.

So as to be dimensionally correct, the lengths of the unit-cell edges were fitted as a^3, b^3 and c^3. The values of K_0/γ reported for each axis therefore correspond with, e.g., $K_a/\gamma = -a^3 (dP/da^3)$. The inter-axial angles often exhibit behaviour that is not readily described by models such as Eq. 1; consequently these have been fitted with polynomials, with due consideration to the temperature derivatives being zero at 0 K (i.e., no linear terms in T) as well as the statistical significance of the coefficients. The fit parameters are given in Supplementary Table S3. Since the measurements on EHA were truncated at 70 K, and we therefore lack the regions of saturation that constrain

quantities such as the Debye temperature, the EHA lattice parameters have been fitted with simple 3rd and 4th order polynomials. These should thus be treated as nothing more than a guide to the eye and of no predictive value outside of the fitted range.

Whilst substantial anisotropy is expected from the reduced dimensionality of the H-bond networks, an accurate representation of the thermal expansion for a triclinic crystal requires determination of the strain tensor, its eigenvalues and eigenvectors. These are, respectively, the magnitudes and directions of the principal directions of the thermal expansion tensor, denoted α_1, α_2 and α_3. Strain tensors between consecutive pairs of lattice parameters were found,[57,58] from which the values of the principal and volumetric thermal expansion coefficients were obtained by standard matrix decomposition methods.

Figure 10 reports the principal linear expansivities and the volume thermal expansion coefficients of EMA and EHA derived using the methods outlined above. The values of α_V at high homologous temperatures, 5 – 6 x10^{-4} K^{-1}, are comparable with other simple alcohol hydrate crystals[3,36] but ~ 50 % greater than that found in methanol mono-ammoniate.[59] It is interesting to note the dramatic change in the thermal expansion of EHA above ~130 K, where both α_1 and α_2 increase sharply and α_3 turns negative. This temperature also corresponds with the onset of substantial size and strain broadening of the Bragg peaks on cooling (*cf.*, Suppl. Fig. S1).

In a triclinic crystal, there are no symmetry restrictions on the orientation of the principal directions, and so these do not typically correspond with the crystallographic axes. In lieu of a long table of direction cosine matrices, and since the orientations of the principal directions do not change substantially with temperature, the most expedient way to understand the directionality of the thermal expansion is from Figure 11. This shows the tensor representation surface[60,61] viewed along the direction of least thermal expansion, α_3, in relation to the unit-cell edges at 175 K. For EMA, the structural relationship is very clear; the largest thermal expansion, α_1, corresponds closely with the weak N1···O1 interaction between the corrugated tapes of 4-sided rings. For EHA, however, the relationship is more obscure. The direction of greatest thermal expansion is canted with respect to planes of H-bonded sheets whilst the direction of negative expansion is approximately aligned with the C1–C2 bond. It may be the case that increasing the interlayer separation on heating permits adjustment of the in-sheet geometry such that the C1 methyl groups interlock more efficiently, contracting the lattice planes perpendicular to α_3. A variable-temperature single-crystal study is required in order to verify this hypothesis.

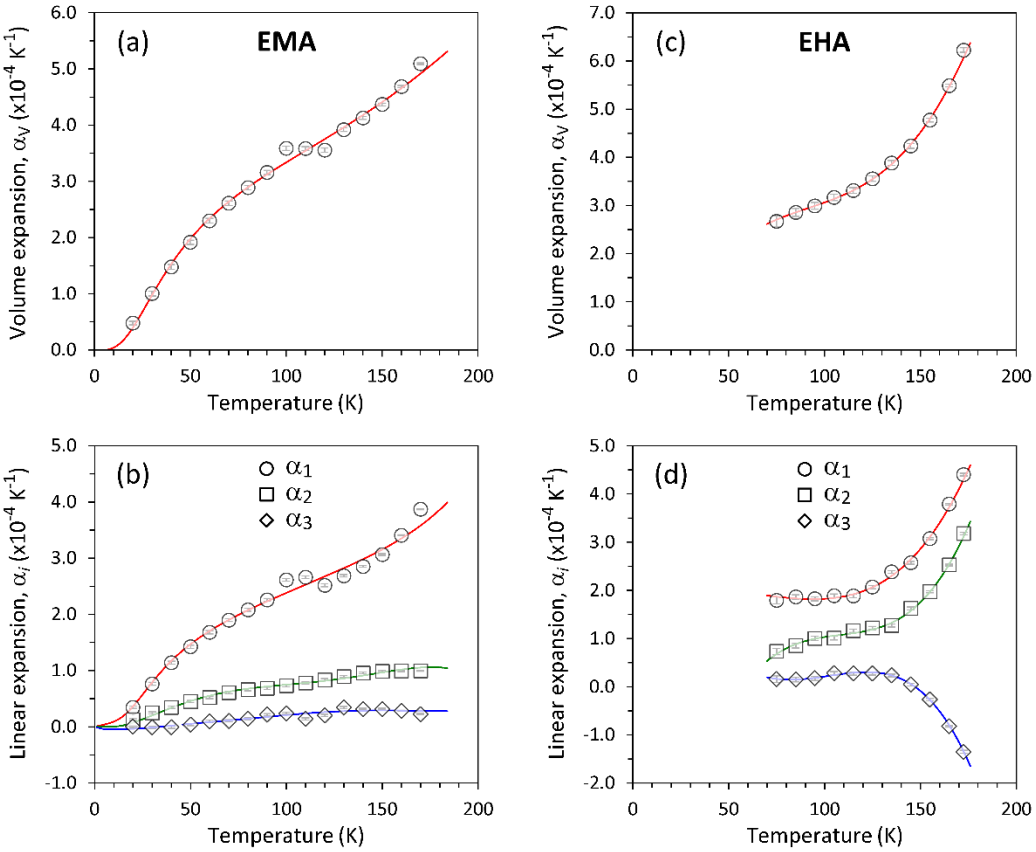

Figure 10

Thermal expansion coefficients: (a) volume expansion and (b) principal linear expansivities of ethanol mono-ammoniate. For the orientation of the principal directions, refer to Figure 11. Symbols represent point-by-point derivatives of the refined unit-cell parameters and solid lines are derived from the fitted models described in the text. The equivalent results for ethanol hemi-ammoniate are shown in (c) and (d).

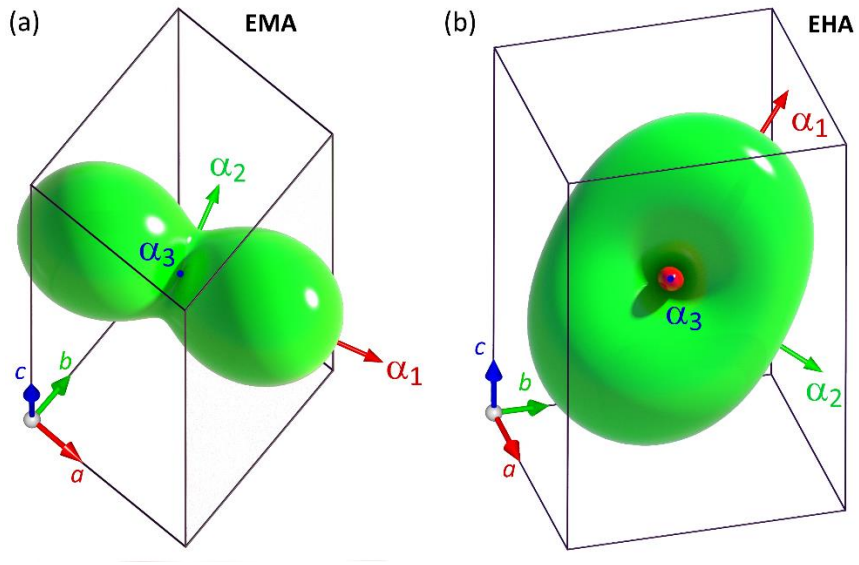

Figure 11

Thermal expansion tensor representation surfaces for ethanol mono-ammoniate (a) and ethanol hemi-ammoniate (b), each evaluated at 175 K and drawn parallel with the direction α_3. The disposition of the unit-cell edges and the two perpendicular principal directions, α_1 and α_2, are indicated. Green surfaces show positive expansivity and red surfaces show negative expansivity.

Thermal expansion of solid ammonia

For the purpose of confirming that the cubic crystal co-existing with EMA in the so-called EDA sample is pure solid ammonia rather than some solid solution, as proposed by Broderson, [16] it is useful to analyse the lattice parameters and thermal expansion of this phase. The temperature dependence of the cubic lattice parameter is given in Suppl. Table S4 and plotted in Fig. 12a. Clearly, these data are in excellent agreement with literature data for ND_3 reported by Olovsson & Templeton[62] and differ from Hewat & Riekel[45] by only 0.2 %. It therefore seems highly likely that this phase is pure ammonia.

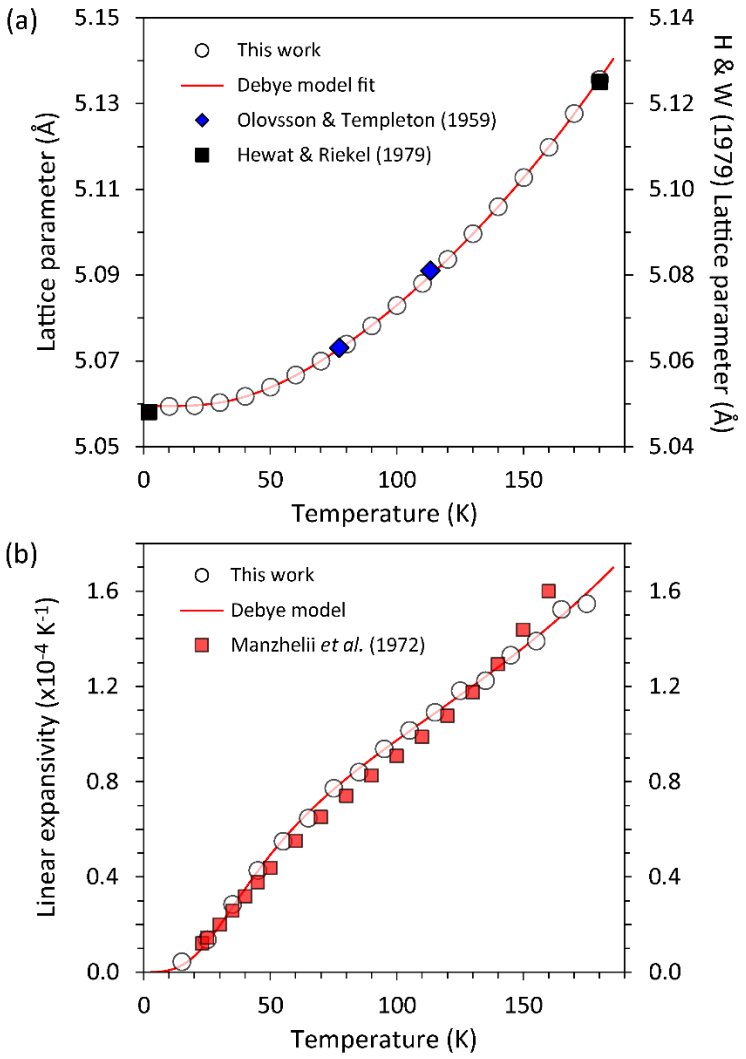

Figure 12

Lattice parameter (a) and linear thermal expansion (b) of solid ammonia obtained in this work and compared with literature data.

The linear expansion coefficients of solid ammonia, NH_3 and ND_3, have been reported previously in the range 23 – 180 K from dilatometry measurements.[63,64] From examination of that work it is not clear how well the sample was thermally equilibrated as the temperature was varied and whether there may have been substantial inhomogeneities in temperature through the sample. Furthermore, there is no obvious correction for sublimation at high homologous temperatures, which can have a measurable effect on the physical dimensions of small volatile samples. As noted

earlier, my thermal protocol pays particular attention to thermal equilibration and precise control during each measurement; moreover, sublimation is of no relevance due to the nature of the bulk crystallographic probe. Nevertheless, there is good agreement between my derived linear expansion coefficient, α_L, for solid deutero-ammonia and those of Manzhelii *et al.*[64] (Fig. 12b).

These data were fitted with the 2nd order Debye model (Eqs. 1 and 2) to produce the solid lines in Figure 12. The resulting fit parameters are: V_0 = 19.4981(5) cm^3 mol^{-1}; θ_D = 206(2) K; K_0/γ = 17.5(2) GPa; K_0' = 17.1(4). The Debye temperature is in reasonable agreement with values of ~220 K obtained from the low-temperature heat capacity[64] and from ultrasonic measurements.[65] The incompressibility of solid ammonia has been determined experimentally[65-67] and computationally,[68] yielding values in the range of 5 – 6 GPa. Since γ is known to be ~1.3 at liquid helium temperatures in solid ND_3,[64] the implied value of K_0 from fitting Eq. 1 is too large by a factor of ~5. This discrepancy is likely due to the very simple model of the vibrational spectrum represented by Eq. 2.

Calculated high pressure behaviours

Geometry optimizations of the EMA and EHA structures were carried out over the range −0.75 to 20 GPa. Supplementary Table S5 compares the zero-pressure unit-cell parameters from the DFT calculations with the nearest available experimental data; 10 K for EMA and 70 K for EHA. It is worth noting that the directions in which the differences are greatest correspond with hydrogen bonded motifs (tapes or sheets) in each structure whereas directions in which the interactions are very weak tend to be reproduced more accurately. This arises due to an overestimation of the H-bond strength by this computational method..

The calculated variation in unit-cell parameters with pressure is shown in Supplementary Figures S4 (EMA) and S5 (EHA) where it may be observed that discontinuities occur in both compounds.

In EMA, the calculations expose a considerable shortening of the very long and weak N–H3···O1 interaction to the point where it develops quickly into a regular hydrogen bond. This coincides with ethanol atom O1 shedding H9, which is transferred to the ammonia molecule to form an ammonium ion (Fig. 13). The effect of this is to shorten the interactions in the $R_2^2(8)$ rings and thus shrink both the *b*-axis and the *c*-axis of the crystal. The resulting salt, ammonium

ethoxide, undergoes no further rearrangement up to 25 GPa and indeed may be 'decompressed' *in silico* down to 2 GPa with only a very minor structural distortion. The curves of total energy as a function of volume, *E*(V), were fitted with integrated forms of a 4th-order logarithmic equation of state:[69]

$$E(P) = V_0\left[\frac{aln^2x}{2} + \frac{bln^3x}{3} + \frac{cln^4x}{4}\right] + E_0 \qquad (3)$$

where V_0 and E_0 are the zero pressure volume and total energy, respectively, $x = V_0/V_P$, and

$$a = K_0 \qquad (4)$$

$$b = \frac{K_0(K_0' - 2)}{2} \qquad (5)$$

$$c = \frac{K_0^2K_0^{"} + K_0 + K_0(K_0' - 2) + K_0(K_0' - 2)^2}{6} \qquad (6)$$

K_0 is the zero-pressure incompressibility (or isothermal bulk modulus); the prime and double-prime terms are the first and second pressure derivatives of K_0, respectively.

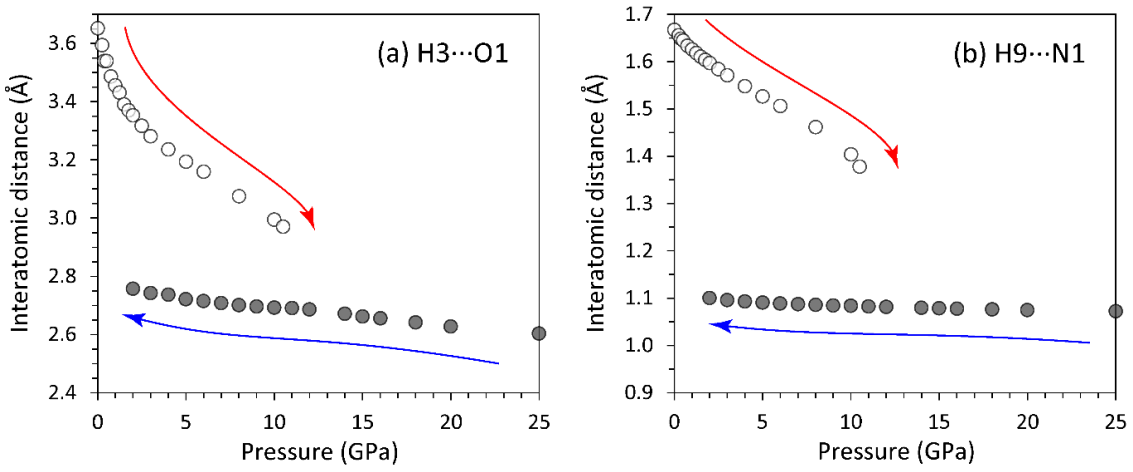

Figure 13

Pressure dependence of two interatomic contacts in ethanol mono-ammoniate derived from DFT geometry optimizations. The open symbols correspond with the molecular form of the crystal and

the filled circles with the ionic form. Arrows indicate calculations done sequentially on pressure increase (red) and decrease (blue). Panel (a) shows the shortening of the very weak N1–H3···O1 intermolecular interaction up to the point where is develops (and then persists) as a 'normal' hydrogen bond. Panel (b) shows the transfer of the hydroxyl hydrogen atom to N to form an ammonium ion.

The fits of Eqs. 3–6 are shown in Figure 14 and the fit parameters are provided in Suppl. Table S6. The enthalpies in the athermal limit, $H = E + PV$, derived from the equation of state and normalised to the enthalpy of the molecular phase, reveal that the thermodynamic equilibrium between the neutral and ionic phases is at 4.46 ± 0.25 GPa (Fig. 15a).

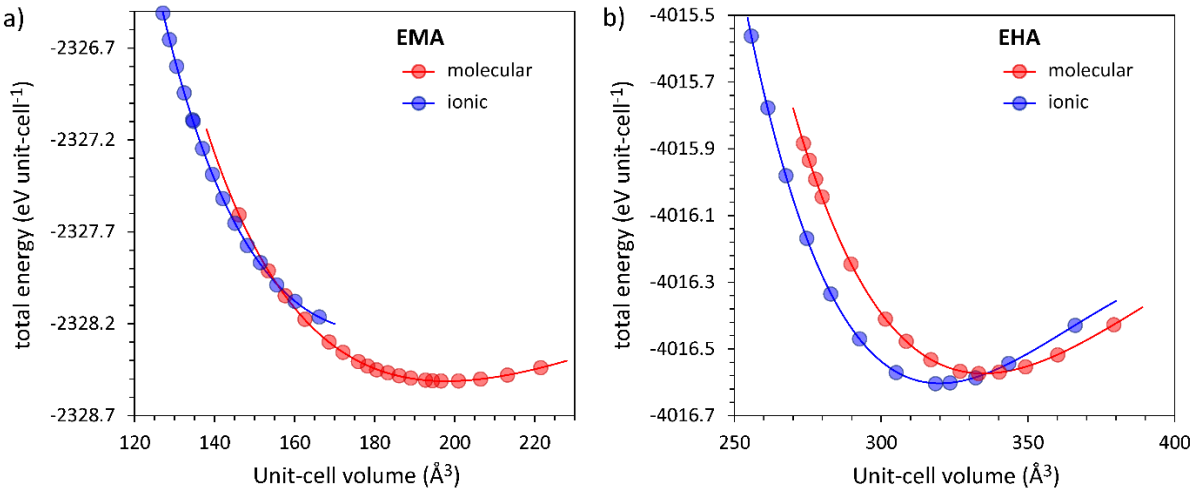

Figure 14

Curves of total electronic energy against unit-cell volume for molecular and ionic phases of ethanol mono-ammoniate (a) and ethanol hemi-ammoniate (b). Symbols are the results of DFT calculations and the solid lines are 4th order logarithmic equations of state (see text).

The discontinuities in the unit-cell parameters of EHA occur at a lower pressure than those in EMA. Nevertheless, the origin of the phenomenon is the same, a proton transfer, although here we find a coupled transfer of two protons. In EHA, there is a proton transfer between the two ethanol molecules (H9 is swapped from O1 to O2) concurrent with a proton transfer between ethanol and ammonia (H15 is swapped from O2 to N1), the result being a partially ionic compound, or ionic co-crystal (according to the currently-accepted definition.[70,71]); ethanol ammonium ethoxide.

Energy-volume curves and enthalpies of the molecular and ionic forms of EMH were computed and fitted with equations of state (Figure 14, Suppl. Table S6). In marked contrast with EMA, the partially ionic form of EHA is found to be the ground state at zero pressure, being lower in enthalpy then the molecular phase by 1.4(8) kJ mol^{-1}. Indeed the thermodynamic equilibrium between the two phases occurs at −0.30 ± 0.24 GPa (Fig. 15b).

The calculated bulk moduli of the two molecular phases, 10.8(2) GPa for EMA and 11.9(2) GPa for EHA, are expected to be ~5 % stiffer than the real materials, by virtue of the *ca*. 1.5 % over-binding produced by the DFT method. The development of shorter, stronger hydrogen-bonded interactions in the ionic phases leads to these crystals having higher zero-pressure bulk moduli; 15(1) GPa for ionic EMA and 14.0(1) GPa for partially ionic EMA.

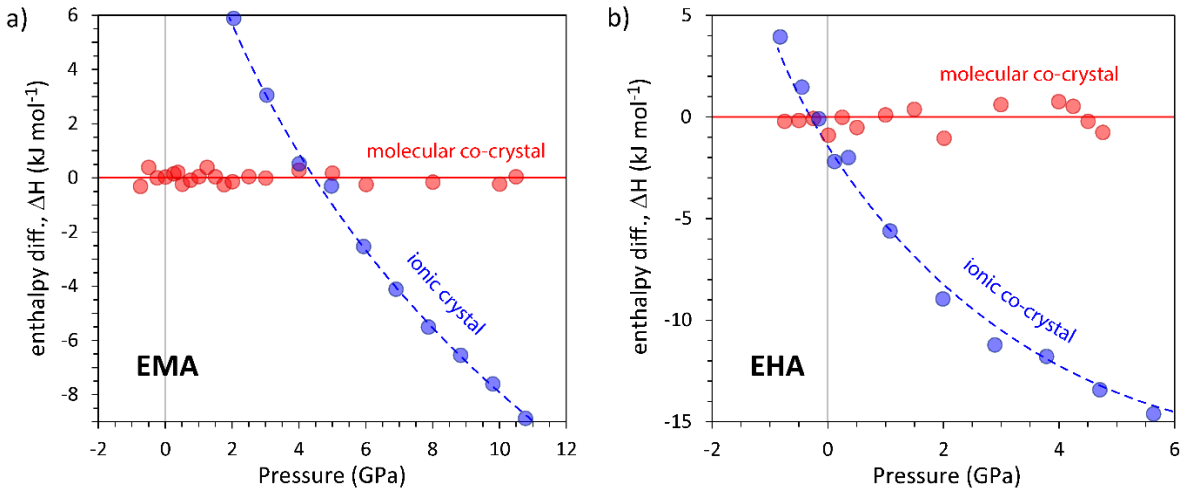

Figure 15

Enthalpies in the athermal limit of the molecular and ionic phases of ethanol mono-ammoniate (a) and ethanol hemi-ammoniate (b), normalised to the enthalpy of the molecular forms. At any particular pressure, the phase with the lowest enthalpy is the thermodynamically stable form. Symbols are the results of DFT calculations and the solid/dashed lines are derived from 4th order logarithmic equations of state (see text).

Concluding remarks

The results of this work confirm Broderson's discovery of ethanol hemi-ammoniate and ethanol mono-ammoniate but do not support the existence of his suggested solid solution. Similarly, the

kink in the mono-ammoniate liquidus on the ammonia-rich side does not appear to be due to the existence of a di-ammoniate (at least in the deuterated material). Hence the ethanol-ammonia binary system[16] is essentially the same as the methanol-ammonia system,[15] comprising the pure end-members, a hemi-ammoniate and mono-ammoniate. This stands in contrast to the much simpler binary systems of ammonia with propanols and butanols,[17] and the more complex binary system of ammonia with phenol.[18,21]

Both of the molecular ammoniates are triclinic, crystallising in space-group $P\bar{1}$. Each is characterised by 4-sided hydrogen bonded rings. In EMA, these form tapes running along the *b*-axis with only dispersion-based interactions between them. In EHA, the 4-sided rings are linked by 6-sided rings to form sheets in the *a*-*b* plane. Like EMA, however, the interactions between the sheets are mediated entirely by dispersion forces.

As a consequence of these highly anisotropic structural elements, the bulk physical properties are also highly anisotropic. The measured thermal expansion of EMA, as well as the calculated incompressibilities of EMA and EHA show that the orientation of the thermal expansion and compressibility maxima correspond with the directions where intermolecular interactions are weakest, as one would expect.

Calculations also indicate that both phases will undergo proton transfer reactions to form a pure salt (EMA → ammonium ethoxide) or an ionic co-crystal (EHA → ethanol ammonium ethoxide). The equilibria for these two reactions are predicted to be at +4.46 GPa and −0.30 GPa, respectively. These results highlight the likely importance of the stoichiometry and the local chemical environment over simple rules based on pK_a differences between the acidic and basic components.[72-75]

I and others have predicted the occurrence of similar complete and partial proton transfer reactions in ammonia hydrates,[76-78] including the transformation of ammonia monohydrate (AMH) to ammonium hydroxide at ~5.5 GPa[79] and ammonia hemihydrate (AHH) to ammonium hydroxide ammoniate at ~12.5 GPa.[78] In reality these processes are interrupted by polymorphic phase transitions at much lower pressures.[80-83] AMH is particularly interesting, however, because the disordered nature of one of the high-pressure molecular phases is known explicitly to hinder the formation of an ionic phase.[84] Clearly, small alcohol molecules offer a more fruitful avenue for permitting proton transfer to ammonia at lower pressures in very simple molecular crystals, where they are less likely to be interrupted by polymorphic transformations.

If this particular combination of DFT methods (ultrasoft pseudopotentials, PBE + TS, convergence criteria) are accurate, then the coupled proton transfer in EMA may occur simply on cooling. Thermally-induced proton transfer is known to occur in other systems.[85] However, considering the relatively low temperature in this instance, the transition could be kinetically-hindered, resulting in the formation only of micro-domains of partially ionic material in a matrix of molecular domains. It is therefore tempting to attribute the substantial size/strain broadening of the Bragg peaks and the large changes in thermal expansion to such a proton transfer. Structure-factor calculations indicate that one would also expect large changes in peak intensities, such as a four-fold increase in the 001 peak at ~9.4 Å and the disappearance of the 100 peak at ~ 5.2 Å for example; such changes are not apparent in the data. It is thus more plausible that the observations collected to date are related to the dynamics of the methyl groups rather than proton transfer but further work is necessary to evaluate these competing hypotheses.

Long-duration studies with protracted periods of annealing may be required in order to achieve substantial degrees of transformation to any partially ionic phase. Simultaneous diffraction and IR or Raman spectroscopic methods affords the opportunity to confirm whether the crystal really exhibits a switch from a molecular to ionic co-crystal on cooling at ambient pressure. Other measurements – ideally with single crystals – will provide insight into the possible role of the methyl groups in the thermal expansion behaviour.

Ionic co-crystals of the form M^+ alkoxide$^-$ alcohol solvate have been known for a long time in metal organic systems,[86-93] the most recent structure to be described being di-ethanol sodium ethoxide in 2020.[94] It is noteworthy that only when M = NH_4 is there a possibility for a purely molecular analogue of the ionic co-crystal to occur and for a transition between the two forms to be observed.

The potential for proton transfer to ammonia from a comparably weak acid such as ethanol at ambient pressure suggests that there may be extensive ammonium salt formation amongst compounds of the simplest alcohols. Even if modest (few GPa) pressures are required, this can readily be generated in hypervelocity impacts. Gaffney and Matson[95] observed that the combination of low shock pressures involved in the production of high-pressure ice polymorphs, the concomitant low post-shock temperatures, and the low ambient temperatures (even at noon at the subsolar point) for all icy objects at or beyond the orbit of Saturn, would lead to the retention of large fractions of shock-induced icy polymorphs. Since many molecular solids are known to

adopt high-pressure structures that may also be preserved on pressure release, provided the temperature is < 150 K, the phenomenon described by Gaffney and Matson will not be restricted only to water ices: shock-induced ionic forms of alcohol ammoniates could also be present in icy regoliths in the outer solar system. This may be an important additional mechanism to reactions with simple carboxylic acids, adsorption onto clay minerals and/or UV photolysis for the generation of NH_4^+ spectroscopic signatures in remotely sensed data from interstellar, cometary and planetary ices.

There is thus a need for both static and dynamic high-pressure studies of these materials in order to determine their likely production, preservation and spectroscopic signatures. There have been some shock equation-of-state studies of water-ammonia-ethanol mixtures carried out recently,[96] with application to the interiors of the ice giant planets, Uranus and Neptune. Furthermore, work on the spectroscopic fingerprints of molecular ices needs to extend beyond single-component substances[97] to the kinds of simple multi-component materials likely to occur in nature, particularly after thermal or shock processing. Having a broad range of well-characterized shock-induced phases that can be detected by remote sensing offers potentially the most robust means of constraining peak shock pressures and post-shock thermal history.

Acknowledgements

I wish to thank the ISIS neutron spallation facility for the equipment and resources used to carry out this work, including the SCARF high-performance computing cluster, as part of beam-time allocation RB 1720183. I thank Dr Sarah Youngs for providing backup ethanol-d_6 at very short notice and Dr Alex Gibbs for helping with the sample preparation.

Data availability

The author declares that all processed numerical data required to support the conclusions of this work are provided in the Supplementary Information.

The raw experimental data are archived at https://doi.org/10.5286/ISIS.E.95699847

Supporting information available:

Supplementary electronic figures and tables.

Crystallographic information files (CIFs) containing the refined structural models and processed data for ethanol mono- and hemi-ammoniate, including CheckCIF reports.
CIFs containing the zero-pressure DFT optimized structures of molecular ethanol mono- and hemi-ammoniate as well as the partially ionic co-crystal of ethanol ammonium ethoxide.

References

(1) Todorova, T.; Delley, B. Molecular crystals: a test system for weak bonding. *J. Phys. Chem. C*. **2010**, 114, 20523–20530. doi:10.1021/jp1049759

(2) Boese, R.; Bläser, D.; Jansen, G. Synthesis and Theoretical Characterization of an Acetylene-Ammonia Cocrystal. *J. Am. Chem. Soc.* **2009**, 131, 2104–2106. doi:10.1021/ja8059705

(3) Fortes, A. D.; Suard, E.; Knight, K. S. Negative linear compressibility and massive anisotropic thermal expansion in methanol monohydrate. *Science* **2011**, 331, 742–746. doi:10.1126/science.1198640

(4) Charnley, S. B.; Kress, M. E.; Tielens, A. G. G. M.; Millar, T. J. Interstellar alcohols. *Astrophys. J.* **1995**, 448, 232–239. doi:10.1086/175955

(5) Rivilla, V. M.; Beltrán, M. T.; Cesaroni, R.; Fontani, F.; Codella, C.; Zhang, Q. Formation of ethylene glycol and other complex organic molecules in star-forming regions. *Astron. Astrophys.* **2017**, 598, article number A59. doi:10.1051/0004-6361/201628373

(6) Allamandola, L. J.; Bernstein, M. P.; Sandford, S. A.; Walker, R. L. Evolution of interstellar ices. In *Composition and Origin of Cometary Materials*. Springer, Dordrecht, **1999**; pp 219–232.

(7) Knacke, R. F.; McCorkle, S.; Puetter, R. C.; Erickson, E. F.; Krätschmer, W. Observation of interstellar ammonia ice. *Astrophys. J.* **1982**, 260, 141–146.

(8) Gürtler, J.; Klaas, U.; Henning, T.; Abrahám, P.; Lemke, D.; Schreyer, K.; Lehmann, K. Detection of solid ammonia, methanol, and methane with ISOPHOT. *Astron. Astrophys.* **2002**, 390, 1075–1087. doi:10.1051/0004-6361:20020772

(9) Biver, N.; Bockelée-Morvan, D.; Moreno, R.; Crovisier, J.; Colom, P.; Lis, D.C.; Sandqvist, A.; Boissier, J.; Despois, D.; Milam, S.N. Ethyl alcohol and sugar in comet C/2014 Q2 (Lovejoy). *Sci. Adv.* **2015**, 1, article number e1500863. doi:10.1126/sciadv.1500863

(10) Bockelée-Morvan, D.; Biver, N. The composition of cometary ices. *Phil. Trans. Roy. Soc. A* **2017**, 375, article number 20160252. doi:10.1098/rsta.2016.0252

(11) Altwegg, K.; Balsiger, H.; Fuselier, S. A. Cometary chemistry and the origin of icy solar system bodies: the view after Rosetta. *Ann. Rev. Astron. Astrophys*. **2019**, 57, 113–55. doi:10.1146/annurev-astro-091918-104409

(12) Shock, E. L.; McKinnon, W. B. Hydrothermal processing of cometary volatiles—Applications to Triton. *Icarus*, **1993**, 106, 464–477. doi:10.1006/icar.1993.1185

(13) Brown, M. E.; Calvin, W. M. Evidence for crystalline water and ammonia ices on Pluto's satellite Charon. *Science* **2000**, 287, 107–109. doi:10.1126/science.287.5450.107

(14) Grundy, W. M.; Binzel, R. P.; Buratti, B. J.; Cook, J. C.; Cruikshank, D. P.; Dalle Ore, C. M.; Earle, A. M. et al. Surface compositions across Pluto and Charon. *Science* **2016**, 351, article number aad9189. doi:10.1126/science.aad9189

(15) Kargel, J. S. Ammonia-water volcanism on icy satellites: Phase relations at 1 atmosphere. *Icarus*, **1992**, 100, 556–574. doi:10.1016/0019-1035(92)90118-Q

(16) Broderson, H. J. *The fusion curve of ammonia and ethyl alcohol*. MA Thesis, University of Kansas, **1911**. http://hdl.handle.net/1808/8452

(17) Cady, H. P.; Jones, E. A. The Fusion Curves for the Systems Ammonia–Propyl Alcohols and Ammonia–Butyl Alcohols. *J. Phys. Chem.* **1933**, 37, 303–320. doi:10.1021/j150345a003

(18) Briner, E.; Agathon, O.; Ferrero, A. Sur les combinaisons d'addition entre les phénols et l'ammoniac I. *Helv. Chim. Acta*, **1926**, 9, 905–912. doi:10.1002/hlca.192600901121

(19) Fortes, A. D.; Wood, I. G.; Knight, K. S. The crystal structure of perdeuterated methanol monoammoniate ($CD_3OD\cdot ND_3$) determined from neutron powder diffraction data at 4.2 and 180 K. *J. Appl. Crystallgr.* **2009**, 42, 1054–1061. doi:10.1107/S0021889809035705

(20) Fortes, A. D.; Wood, I. G.; Knight, K. S. (2010). The crystal structure of perdeuterated methanol hemiammoniate ($CD_3OD\cdot 0.5ND_3$) determined from neutron powder diffraction data at 4.2 and 180 K. *J. Appl. Crystallgr.* **2010**, 43, 328–336. doi:10.1107/S0021889810005595

(21) Fortes, A. D. *Structures of phenol-ammonia and phenol-water compounds*. STFC ISIS Neutron and Muon Source, **2019**, RB1920009. doi:10.5286/ISIS.E.RB1920009

(22) Ibberson, R.M. Design and performance of the new supermirror guide on HRPD at ISIS. *Nucl. Instr. Methods A* **2009**, 600, 47–49. doi:10.1016/j.nima.2008.11.066

(23) Arnold, O., & 27 co-authors. Mantid—Data analysis and visualization package for neutron scattering and μSR experiments. *Nucl. Instrum. Methods A* **2014**, 764, 156–166. doi:10.1016/j.nima.2014.07.029

(24) Albinati, A.; Willis, B. T. M. The Rietveld method in neutron and X-ray powder diffraction. *J. Appl. Crystallogr.* **1982**, 15, 361–374. doi:10.1107/S0021889882012187

(25) Le Bail, A. Whole powder pattern decomposition methods and applications: A retrospection. *Powder Diffr.* **2005**, 20, 316–326. doi:10.1154/1.2135315

(26) Larson, A. C.; Von Dreele, R. B. *General Structure Analysis System (GSAS)*. Los Alamos National Laboratory Report, LAUR 86-748, **1994**.

(27) Toby, B. H. EXPGUI, a graphical user interface for GSAS. *J. Appl. Crystallogr.* **2001**, 34, 210–213. doi:10.1107/S0021889801002242

(28) Hohenberg, P.; Kohn, W. Inhomogeneous electron gas. *Phys. Rev*. **1964,** 136, B864–B871. doi:10.1103/PhysRev.136.B864

(29) Kohn, W.; Sham, L. J. Self-consistent equations including exchange and correlation effects. *Phys. Rev*. **1965**, 140, A1133–A1138. doi:10.1103/PhysRev.140.A1133

(30) Payne, M. C.; Teter, M. P.; Allan, D. C.; Arias, T. A.; Joannopoulos, J. D. Iterative minimization techniques for *ab initio* total-energy calculations: molecular dynamics and conjugate gradients. *Rev. Mod. Phys*. **1992**, 64, 1045–1097. doi:10.1103/RevModPhys.64.1045

(31) Segall, M. D.; Lindan, P. J. D.; Probert, M. J.; Pickard, C. J.; Hasnip, P. J.; Clark, S. J.; Payne, M. C. First-principles simulation: ideas, illustrations and the CASTEP code. *J. Phys. Cond. Matter* **2002**, 14, 2717–2744. doi:10.1088/0953-8984/14/11/301

(32) Clark, S. J.; Segall, M. D.; Pickard, C. J.; Hasnip, P. J.; Probert, M. I. J.; Refson, K.; Payne, M. C. First principles methods using CASTEP. *Z. Krist*. **2005**, 220, 567–570. doi:10.1524/zkri.220.5.567.65075

(33) Perdew, J. P.; Burke, K.; Ernzerhof, M. Generalized gradient approximation made simple. *Phys. Rev. Lett.* **1996**, 77, 3865–3868. doi:10.1103/PhysRevLett.77.3865

(34) Perdew, J. P.; Burke, K.; Ernzerhof, M. Generalized gradient approximation made simple. *Phys. Rev. Lett.* **1997**, 78, 1396. doi:10.1103/PhysRevLett.78.1396

(35) Tkatchenko,A.; Scheffler, M. Accurate molecular van der Waals interactions from ground-state electron density and free-atom reference data. *Phys. Rev. Lett.*, **2009**, 102, 073005–073008. doi:10.1103/PhysRevLett.102.073005

(36) Fortes, A. D. Phenol hemihydrate: redetermination of the crystal structure by neutron powder diffraction, Hirschfeld surface analysis and characterization of the thermal expansion. *Acta Crystallogr. E* **2020**, 76, 1062–1069. doi:10.1107/S2056989020007719

(37) Pfrommer, B. G.; Cote, M.; Louie, S. G.; Cohen, M. L. Relaxation of crystals with the Quasi-Newton method. *J. Comp. Phys*. **1997**, 191, 233–240. doi:10.1006/jcph.1996.5612
(38) Rutter, M. J. C2X: A tool for visualisation and input preparation for Castep and other electronic structure codes. *Comput. Phys. Comm*. **2018**, 225, 174–179. doi:10.1016/j.cpc.2017.12.008
(39) Momma, K.; Izumi, F. VESTA 3 for three-dimensional visualization of crystal, volumetric and morphology data. *J. Appl. Cryst*. **2011**, 44, 1272–1276. doi:10.1107/S0021889811038970
(40) Vega, D.; Almeida, D. AIM-UC: An application for QTAIM analysis. *J. Comput. Meth. Sci. Eng.* **2014**, 14, 131–136. doi:10.3233/JCM-140491
(41) Louër, D.; Boultif, A. Powder pattern indexing and the dichotomy algorithm. *Z. Kristallogr. Suppl.* **2007**, 26, 191–196. doi:10.1524/9783486992540-030
(42) De Wolff, P.M. (1968): A simplified criterion for the reliability of a powder pattern indexing. *J. Appl. Crystallogr*. **1968**, 5, 108–113. doi:10.1107/S002188986800508X
(43) Smith, G. S.; Snyder, R. L. F(N): a criterion for rating powder diffraction patterns and evaluating the reliability of powder-pattern indexing, *J. Appl. Crystallogr.* **1979**, 12, 60–65. doi:10.1107/S002188987901178X
(44) Jönsson, P. G. Hydrogen bond studies. CXIII. The crystal structure of ethanol at 87 K. *Acta Crystallogr. B* **1976**, 32, 232–235. doi:10.1107/S0567740876002653
(45) Hewat, A. W.; Riekel, C. The crystal structure of deuteroammonia between 2 and 180 K by neutron powder profile refinement. *Acta Crystallogr. A* **1979**, 35, 569–571. doi:10.1107/S0567739479001340
(46) Favre-Nicolin, V.; Černý, R. FOX, 'free objects for crystallography': a modular approach to *ab initio* structure determination from powder diffraction. *J. Appl. Crystallogr*. **2002**, 35, 734–743. doi:10.1107/S0021889802015236
(47) Favre-Nicolin, V.; Černý, R. A better FOX: using flexible modeling and maximum likelihood to improve direct-space *ab initio* structure determination from powder diffraction. *Z. Krist*. **2004**, 219, 847–856. doi:10.1524/zkri.219.12.847.55869
(48) Etter, M. C.; MacDonald, J. C.; Bernstein, J. Graph-set analysis of hydrogen-bond patterns in organic crystals. *Acta Crystallogr. B.* **1990**, 46, 256–262. doi:10.1107/S0108768189012929

(49) Mantina, M.; Chamberlin, A. C.; Valero, R.; Cramer, C. J.; Truhlar, D. G. Consistent van der Waals radii for the whole main group. *J. Phys. Chem. A* **2009**, 113, 5806–5812. doi:10.1021/jp8111556

(50) Wick, C. R.; Clark, T. On bond-critical points in QTAIM and weak interactions. *J. Mol. Model*. **2018**, 24, article number 142. doi:10.1007/s00894-018-3684-x

(51) Jabłoński, M. On the uselessness of bond paths linking distant atoms and on the violation of the concept of privileged exchange channel. *Chem. Open*. **2019**, 8, 497–507. doi:10.1002/open.201900109

(52) Shahbazian, S. Why bond critical points are not "bond" critical points. *Chem. Eur. J*. **2018**, 24, 5401–5405. doi:10.1002/chem.201705163

(53) Taylor, R. Identifying intermolecular atom···atom interactions that are not just bonding but also competitive. *CrystEngComm*. **2020**, doi:10.1039/d0ce00270d

(54) Desiraju, G. R. The C–H···O hydrogen bond in crystals: what is it? *Acc. Chem. Res*. **1991**, 24, 290–296. doi:10.1021/ar00010a002

(55) Steiner, T.; Desiraju, G. R. Distinction between the weak hydrogen bond and the van der Waals interaction. *Chem. Comm*. **1998**, 891–892. doi:10.1039/A708099I

(56) Koch, U.; Popelier, P. L. A. Characterization of C–H–O hydrogen bonds on the basis of the charge density. *J. Phys. Chem.* **1995**, 99, 9747–9754. doi:10.1021/j100024a016

(57) Ohashi, Y.; Burnham , C. W. Clinopyroxene lattice deformations: The roles of chemical substitution and temperature. *Am. Mineral.* **1973**, 58, 843–849.

(58) Ohashi, Y. A program to calculate the strain tensor from two sets of unit-cell parameters. In, Hazen, R. M. and Finger, L. W., *Comparative Crystal Chemistry*. Wiley, New York, **1982**; pp 92–102.

(59) Fortes, A. D.; Adams, M.; Knight, K. S.; Wood, I. G. *Thermal expansion and simultaneous Raman spectroscopy of methanol ammoniates, $CD_3OD{\cdot}ND_3$ and $2CD_3OD{\cdot}ND_3$.* STFC ISIS Neutron and Muon Source, **2010**, RB1010210. doi:10.5286/ISIS.E.24079379

(60) Hashash, Y. M.; Yao, J. I. C.; Wotring, D. C. Glyph and hyperstreamline representation of stress and strain tensors and material constitutive response. *Int. J. Num. Anal. Methods Geomech*. **2003**, 27, 603–626. doi:10.1002/nag.288

(61) WinTensor. http://cad4.cpac.washington.edu/WinTensorhome/WinTensor.htm

(62) Olovsson, I.; Templeton, D. H. X-ray study of solid ammonia. *Acta Crystallogr*. **1959**, 12, 832–836. doi:10.1107/S0365110X59002420

(63) Manzhelii, V. G.; Tolkachev, A. M. Тепловое Расширение Кристаллического Аммиака. *Fiz. Tverd. Tela* **1966**, 8, 1035–1039.

(64) Manzhelii, V. G.; Tolkachev, A. M.; Krupskii, I. N.; Voitovich, E. I.; Popov, V. A.; Koloskova, L. A. Thermal properties of solid ND_3. *J. Low Temp. Phys.* **1972**, 7, 169–182. doi:10.1007/BF00629127

(65) Voitovich, E. I.; Tolkachev, A. M.; Manzhelli, V. G. Adiabatic compressibility of solid gases. *J. Low. Temp. Phys*. **1971**, 5, 435–446. doi:10.1007/BF00629536

(66) Powell, B. M.; Dolling, G.; Pawley, G. S.; Leech, J. W. Lattice dynamics of ammonia. *Can. J. Phys*. **1980**, 58, 1703–1711. doi:10.1139/p80-227

(67) Kiefte, H.; Breckon, S. W.; Penney, R.; Clouter, M. J. Elastic constants of ammonia by Brillouin spectroscopy. *J. Chem. Phys*. **1985**, 83, 4738–4743. doi:10.1063/1.448999

(68) Fortes, A. D.; Brodholt, J. P.; Wood, I. G.; Vočadlo, L. Hydrogen bonding in solid ammonia from *ab initio* calculations. *J. Chem. Phys*, **2003**, 118, 5987–5994. doi:10.1063/1.1555630

(69) Poirier, J. P.; Tarantola, A. A logarithmic equation of state. *Phys. Earth Planet. Int.* **1998**, 109, 1–8. doi:10.1016/S0031-9201(98)00112-5

(70) Grothe, E.; Meekes, H.; Vlieg, E.; Ter Horst, J. H.; de Gelder, R. D. Solvates, salts, and cocrystals: a proposal for a feasible classification system. *Cryst. Growth. Des.* **2016**, 16, 3237–3243. doi:10.1021/acs.cgd.6b00200

(71) Zhang, C.; Xiong, Y.; Jiao, F.; Wang, M.; Li, H. Redefining the term “cocrystal” and broadening its intention. *Cryst. Growth Des*. **2019**, 19, 1471–1478. doi:10.1021/acs.cgd.8b01537

(72) Cruz-Cabeza, A. J. Acid–base crystalline complexes and the pKa rule. *CrystEngComm* **2012**, 14, 6362–6365. doi:10.1039/C2CE26055G

(73) Pratik, S. M.; Datta, A. Nonequimolar mixture of organic acids and bases: an exception to the rule of thumb for salt or cocrystal. *J. Phys. Chem. B* **2016**, 120, 7606–7613. doi:10.1021/acs.jpcb.6b05830

(74) Sedghiniya, S.; Soleimannejad, J.; Janczak, J. The salt–cocrystal spectrum in salicylic acid–adenine: the influence of crystal structure on proton-transfer balance. *Acta Crystallogr. C* **2019**, 75, 412–421. doi:10.1107/S205322961900312

(75) Kavanagh, O.; Walker, G.; Lusi, M. Graph-set analysis helps to understand charge transfer in novel ionic cocrystal when the ΔpKa rule fails. *Cryst. Growth Des*. **2019**, 19, 5308–5313. doi:10.1021/acs.cgd.9b00770

(76) Griffiths, G. I. G.; Misquitta, A. J.; Fortes, A. D.; Pickard, C. J.; Needs, R. J. High pressure ionic and molecular crystals of ammonia monohydrate within density functional theory. *J. Chem. Phys.* **2012**, 137, article number 064506. doi:10.1063/1.4737887

(77) Jiang, X.; Wu, X.; Zheng, Z.; Huang, Y.; Zhao, J. Ionic and superionic phases in ammonia dihydrate $NH_3{\cdot}2H_2O$ under high pressure. *Phys. Rev. B* **2017**, 95, article number 144104. doi:10.1103/PhysRevB.95.144104

(78) Naden Robinson, V.; Marqués, M.; Wang, Y.; Ma, Y.; Hermann, A. Novel phases in ammonia-water mixtures under pressure. *J. Chem. Phys.* **2018**, 149, article number 234501. doi:10.1063/1.5063569

(79) Fortes, A. D.; Brodholt, J. P.; Wood, I. G.; Vočadlo, L.; Jenkins, H. D. B. *Ab initio* simulation of ammonia monohydrate ($NH_3{\cdot}H_2O$) and ammonium hydroxide (NH_4OH). *J. Chem. Phys.* **2001**, 115, 7006–7014. doi:10.1063/1.1398104

(80) Fortes, A. *Experimental and computational studies of solids in the ammonia-water system*. PhD thesis, University of London, 2004.

(81) Fortes, A. D.; Wood, I. G.; Vočadlo, L.; Knight, K. S.; Marshall, W. G.; Tucker, M. G.; Fernandez-Alonso, F. Phase behaviour and thermoelastic properties of perdeuterated ammonia hydrate and ice polymorphs from 0 to 2 GPa. *J. Appl. Crystallogr.* **2009**, 42, 846–866. doi:10.1107/S0021889809027897

(82) Fortes, A. D.; Suard, E.; Lemée-Cailleau, M. H.; Pickard, C. J.; Needs, R. J. Crystal structure of ammonia monohydrate phase II. *J. Am. Chem. Soc.* **2009**, 131, 13508–13515. doi:10.1021/ja9052569

(83) Griffiths, G. I. G.; Fortes, A. D., Pickard, C. J.; Needs, R. J. Crystal structure of ammonia dihydrate II. *J. Chem. Phys.* **2012**, 136, article number 174512. doi:10.1063/1.4707930

(84) Liu, C.; Mafety, A.; Queyroux, J. A.; Wilson, C. W.; Zhang, H.; Béneut, K.; Le Marchand, G.; Baptiste, B.; Dumas, P.; Garbarino, G.; Finocchi, F.; Loveday, J. S.; Pietrucci, F., Saitta, A. M.; Datchi, F.; Ninet, S. Topologically frustrated ionisation in a water-ammonia ice mixture. *Nature Comms.* **2017**, 8, 1–8. doi:10.1038/s41467-017-01132-z

(85) Jones, C. L.; Skelton, J. M.; Parker, S. C.; Raithby, P. R.; Walsh, A.; Wilson, C. C.; Thomas, L. H. Living in the salt-cocrystal continuum: indecisive organic complexes with thermochromic behaviour. *CrystEngComm* **2019**, 21, 1626–1634. doi:10.1039/C8CE02066C

(86) Mehring, M.; Berkei, M.; Schürmann, M. Crystal structure of LiO^{i}Pr·5^{i}PrOH—a hydrogen-bonded chain structure. *Z. Anorg. Allgem. Chem*. **2002**, 628, 1975–1978. doi:10.1002/1521-3749(200209)628:9/10<1975::AID-ZAAC1975>3.0.CO;2-I

(87) Starikova, Z. A.; Yanovsky, A. I.; Turevskaya, E. P.; Turova, N. Y. The structure of the crystal solvate of magnesium methoxide with methanol, $Mg(OMe)_2$·3.5MeOH. *Polyhedron* **1997**, 16, 967–974. doi:10.1016/S0277-5387(96)00339-7

(88) Starikova, Z. A.; Turevskaya, E. P.; Turova, N. Y.; Yanovsky, A. I. The structure of the LiOMe·2MeOH crystal solvate. A new structural type for tetrameric alkoxides. *J. Chem. Soc., Dalton Trans*. **2000**, 19, 3237–3238. doi:10.1039/B005782G

(89) Starikova, Z. A.; Turevskaya, E. P.; Turova, N. Y.; Yanovsky, A. I. On the structure of heterometallic methoxide $Li_2(WO)_2(OMe)_{10}$·MeOH. *Polyhedron* **2002**, 21, 193–195. doi:10.1016/S0277-5387(01)00981-0

(90) Chisholm, M. H.; Drake, S. R.; Naiini, A. A.; Streib, W. E. Synthesis and X-ray crystal structures of the one-dimensional ribbon chains [MOBu^{t}·Bu^{t}OH]∞ and the cubane species [MOBu^{t}]$_4$ (M = K and Rb). *Polyhedron* **1991**, 103, 337–345. doi:10.1016/S0277-5387(00)80154-0

(91) Kessler, V. G.; Turevskaya, E. P.; Turova, N. Y. Interaction of magnesium and niobium methoxides. X-ray single crystal study of $Mg_2Nb_2O_2(OMe)_{10}(MeOH)_4$. *Polyhedron* **2002**, 21, 1629–1634. doi:10.1016/S0277-5387(02)01034-3

(92) Kessler, V. G.; Turova, N. Y.; Turevskaya, E. P. The structure of the bismuth ethoxide ethanol solvate. A new structural type for octameric alkoxides. *Inorg. Chem. Comm*. **2002**, 5, 549–551. doi:10.1016/S1387-7003(02)00478-1

(93) Dinnebier, R. E.; Pink, M.; Sieler, J.; Norby, P.; Stephens, P. W. Powder Structure Solutions of the Compounds Potassium Phenoxide−Phenol: C_6H_5OK·$x$$C_6H_5OH$ (x = 2, 3). *Inorg. Chem*. **1998**, 37, 4996–5000. doi:10.1021/ic980350a

(94) Beske, M.; Tapmeyer, L.; Schmidt, M. U. (2020). Crystal structure of sodium ethoxide (C_2H_5ONa), unravelled after 180 years. *Chem. Comm*. **2020**, 56, 3520–3523. doi:10.1039/C9CC08907

(95) Gaffney, E. S.; Matson, D. L. Water ice polymorphs and their significance on planetary surfaces. *Icarus* **1980**, 44, 511–519. doi:10.1016/0019-1035(80)90041-X

(96) Guarguaglini, M.; Hernandez, J. –A.; Okuchi, T.; Barroso, P.; Benuzzi-Mounaix, A.; Bethkenhagen, M.; Bolis, R.; Brambrink, E.; French, M.; Fujimoto, Y.; Kodama, R.; Koenig, M.; Lefevre, F.; Myanishi, K.; Ozaki, N.; Redmer, R.; Sano, T.; Umeda, Y.; Vinci, T.; Ravasio, A. Laser-driven shock compression of "synthetic planetary mixtures" of water, ethanol, and ammonia. *Sci. Rep*. **2019**, 9, article number 10155. doi:10.1038/s41598-019-46561-6

(97) Hudson, R. L.; Loeffler, M. J.; Ferrante, R. F.; Gerakines, P. A.; Coleman, F. M. Testing densities and refractive indices of extraterrestrial ice components using molecular structures – organic compounds and molar refractions. *Astrophys. J*. **2020**, 891, article number 22. doi:10.3847/1538-4357/ab6efa

TOC graphic

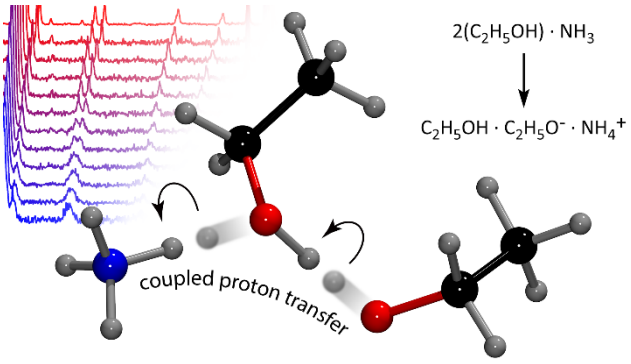

Co-crystals, salts and ionic co-crystals of ethanol and ammonia

A. Dominic Fortes,[1,2,*]

[1] ISIS Neutron & Muon Spallation Source, Rutherford Appleton Laboratory, Harwell Science and Innovation Campus, Chilton, Oxfordshire, OX11 0QX, United Kingdom.

[2] Department of Earth Sciences, University College London, Gower Street, London WC1E 6BT, United Kingdom.

*Corresponding author email: dominic.fortes@stfc.ac.uk

Supplementary Figures

Figure S1

Stack-plot of neutron powder diffraction data collected from ethanol hemi-ammoniate. The uppermost profile reports the long measurement at 175 K that was used for the structure refinement. Subsequent profiles moving down the stack are at 170 K and then in 10 K increments to 70 K. The bottom profile (70 K) appears noisier due to a shorter counting time.

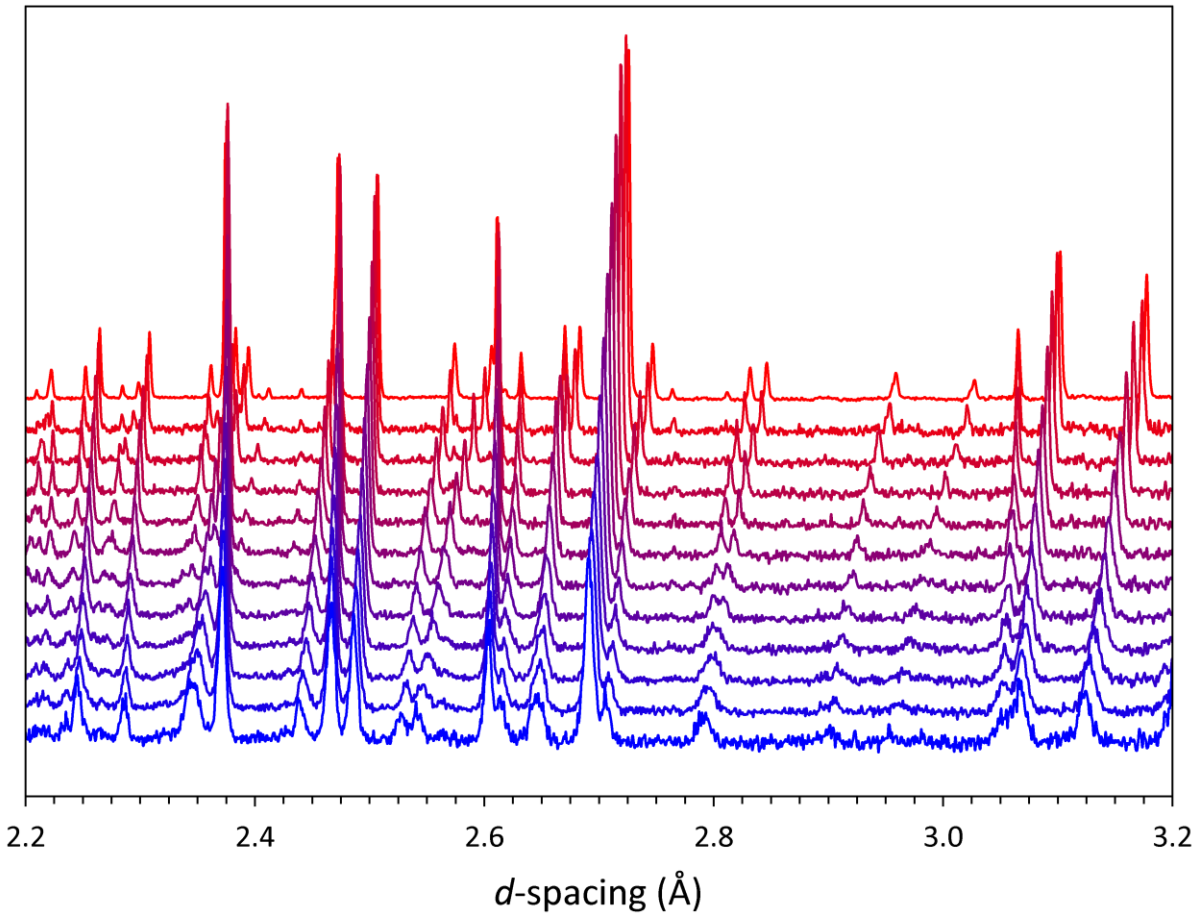

Figure S2

Unit-cell parameters of ethanol mono-ammoniate between 10 and 180 K: (a) *a*-axis; (b) *b*-axis; (c) *c*-axis; (d) angle α; (e) angle β; (f) angle γ; (g) unit-cell volume (overleaf). Open circles represent the observations and the solid lines are Debye model or polynomial fits (see main text and Table S3)

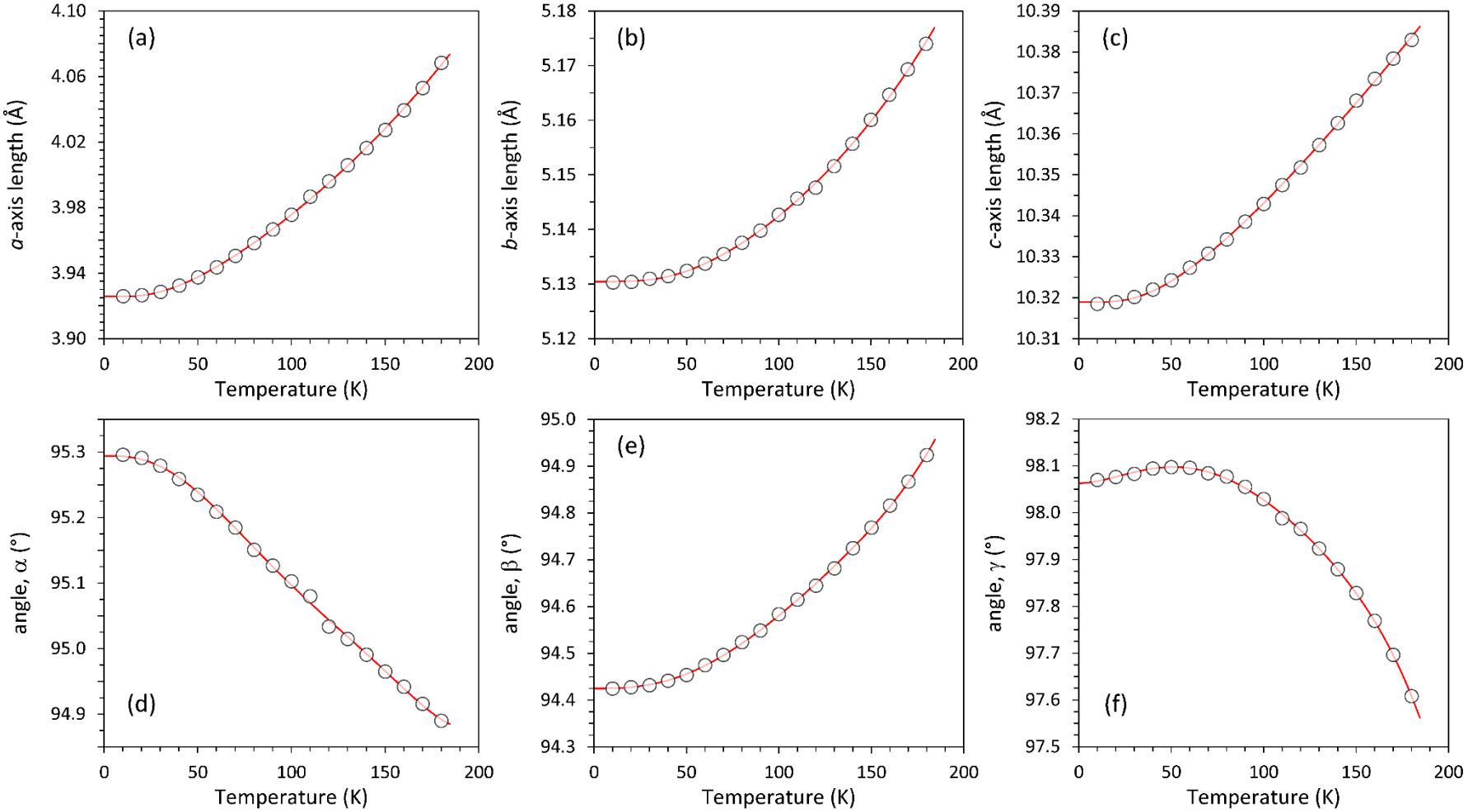

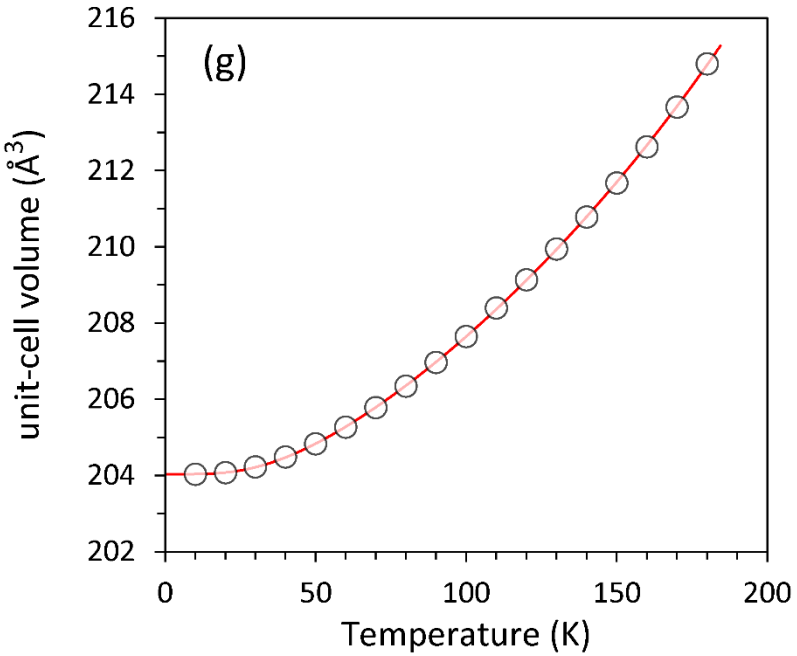
(g)
unit-cell volume (Å^3)
216
214
212
210
208
206
204
202
0
50
100
150
200
Temperature (K)

Figure S3

Unit-cell parameters of ethanol hemi-ammoniate between 70 and 175 K: (a) *a*-axis; (b) *b*-axis; (c) *c*-axis; (d) angle α; (e) angle β; (f) angle γ; (g) unit-cell volume (overleaf). Open circles represent the observations and the solid lines are polynomial fits (see main text)

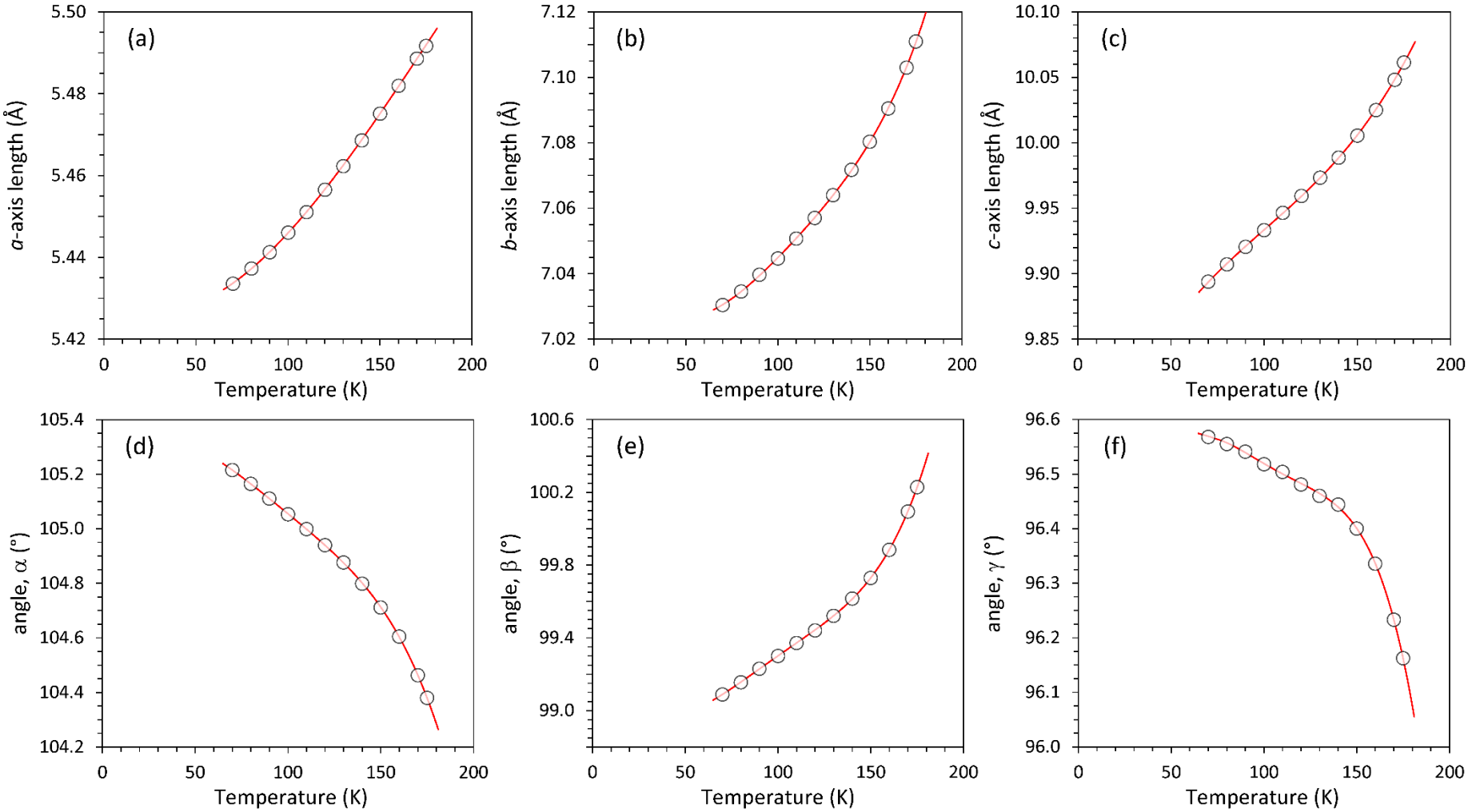

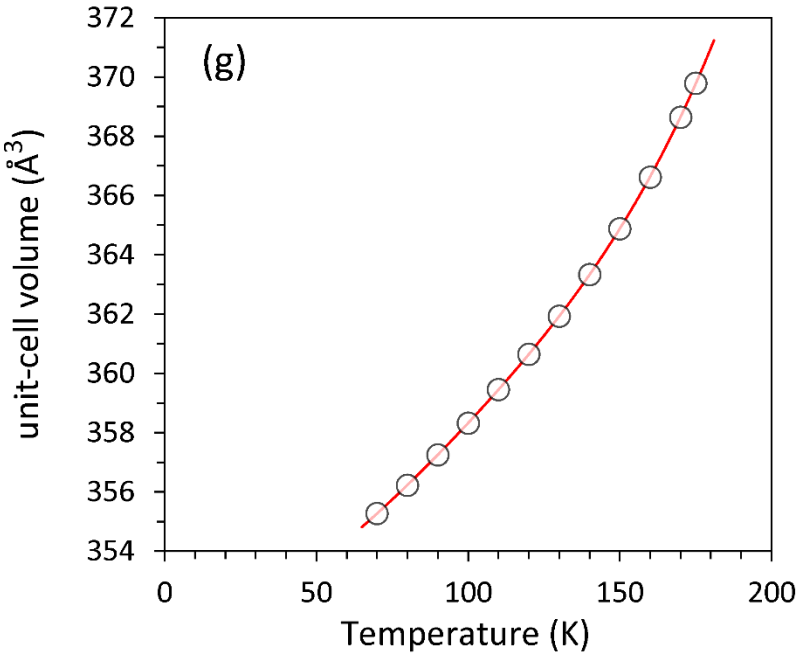
(g)
unit-cell volume (Å^3)
372
370
368
366
364
362
360
358
356
354
0
50
100
150
200
Temperature (K)

Figure S4

Unit-cell parameters of ethanol mono-ammoniate obtained from DFT calculations over the range of pressures 0 – 25 GPa: (a) *a*-axis; (b) *b*-axis; (c) *c*-axis; (d) angle α; (e) angle β; (f) angle γ; (g) unit-cell volume (overleaf). Open circles correspond with the molecular co-crystal and filled circles correspond to the ionic crystal.

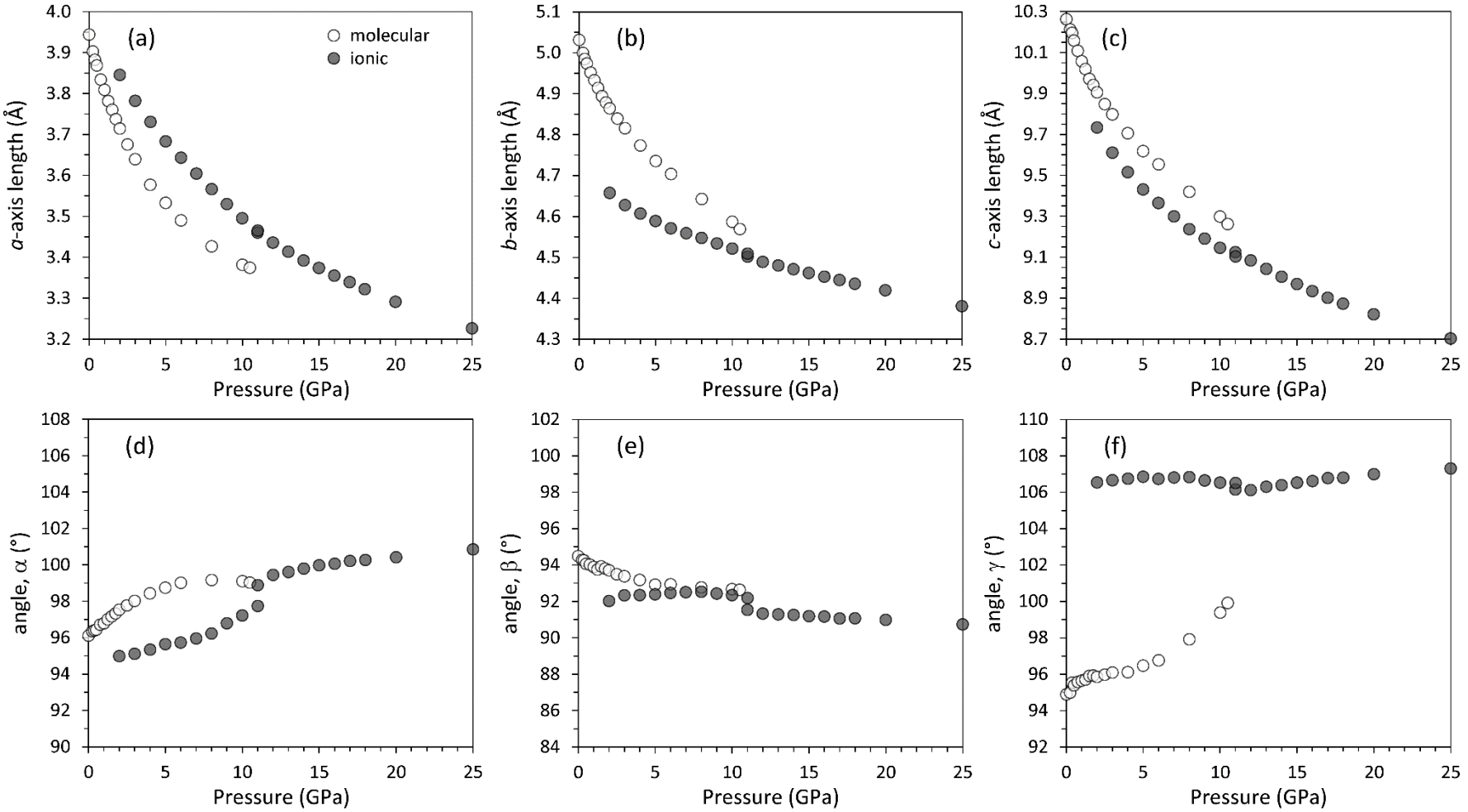

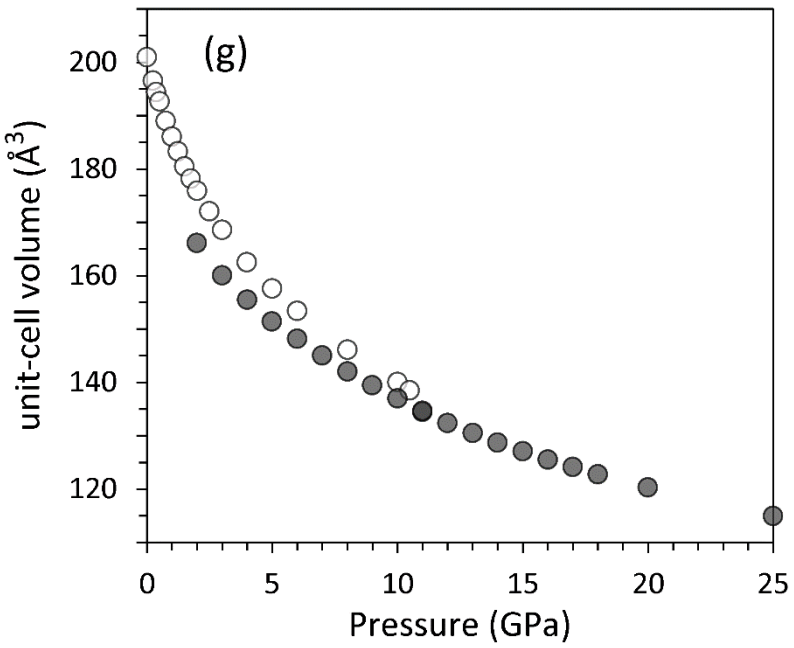
(g)
unit-cell volume (Å^3)
200
180
160
140
120
0
5
10
15
20
25
Pressure (GPa)

Figure S5

Unit-cell parameters of ethanol hemi-ammoniate obtained from DFT calculations over the range of pressures 0 – 20 GPa: (a) *a*-axis; (b) *b*-axis; (c) *c*-axis; (d) angle α; (e) angle β; (f) angle γ; (g) unit-cell volume (overleaf). Open circles correspond with the molecular co-crystal and filled circles correspond to the ionic co-crystal.

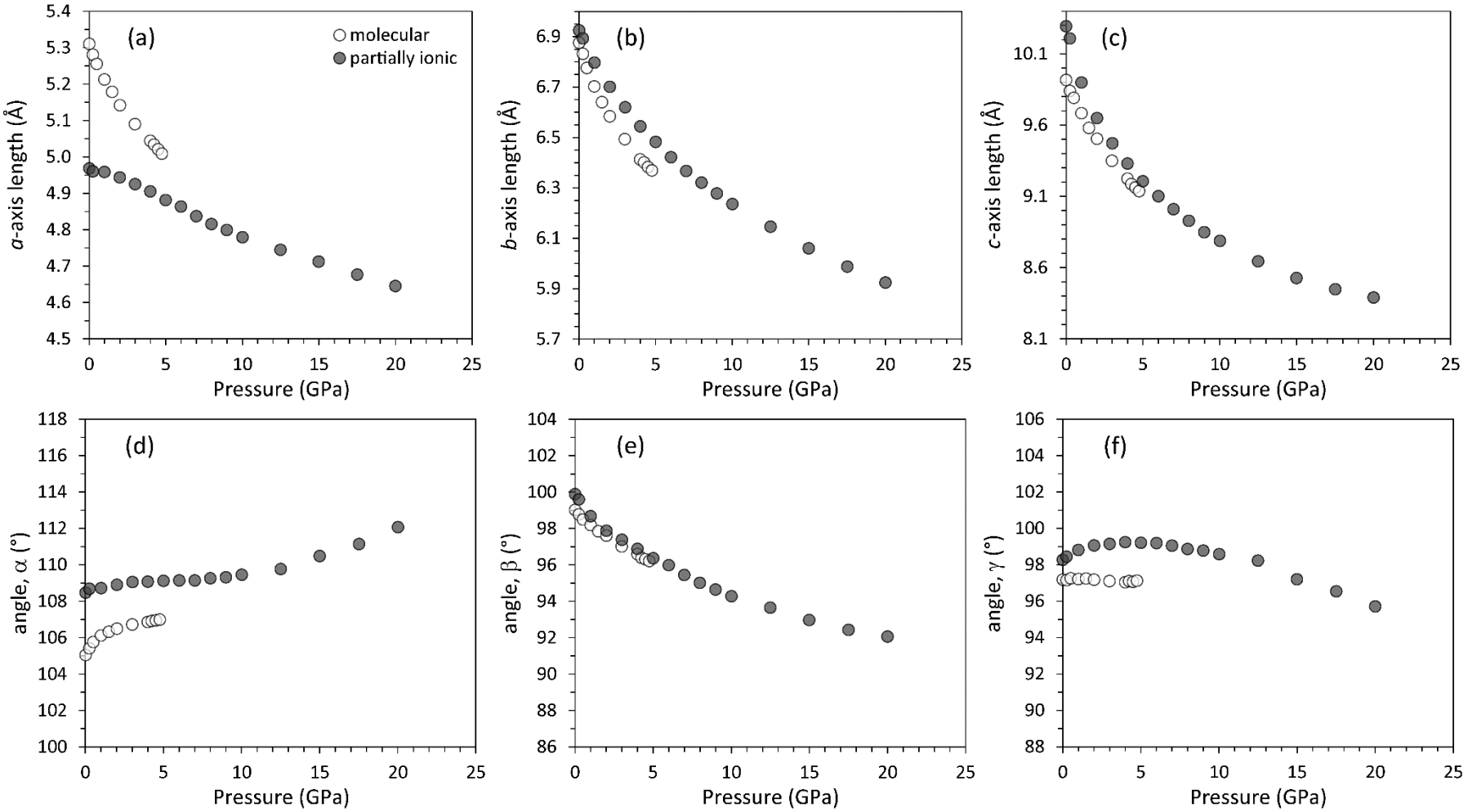

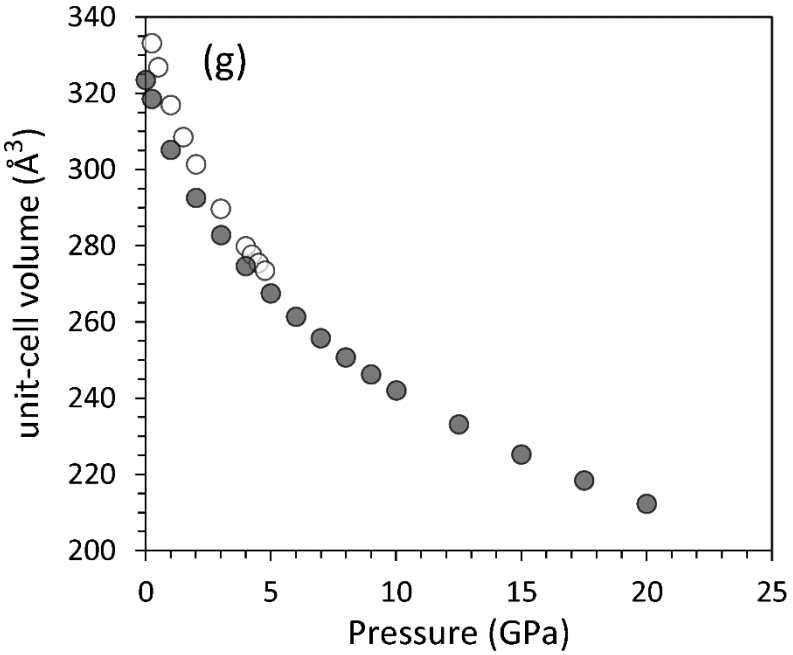
(g)
unit-cell volume (Å^3)
340
320
300
280
260
240
220
200
0
5
10
15
20
25
Pressure (GPa)

Table S1

Refined unit-cell parameters of ethanol mono-ammoniate. These data are plotted in Fig. S2.

T (K)	*a* (Å)	*b* (Å)	*c* (Å)	α (°)	β (°)	γ (°)	V (Å^3)
180	4.06831(2)	5.17400(2)	10.38296(4)	94.8905(4)	94.9238(4)	97.6082(3)	214.796(1)
170	4.05297(3)	5.16932(3)	10.37842(6)	94.916(1)	94.867(1)	97.696(1)	213.664(2)
160	4.03938(3)	5.16469(3)	10.37348(6)	94.942(1)	94.816(1)	97.769(1)	212.626(2)
150	4.02744(3)	5.16011(3)	10.36812(7)	94.965(1)	94.769(1)	97.828(1)	211.676(2)
140	4.01635(4)	5.15569(4)	10.36266(9)	94.991(1)	94.725(1)	97.879(1)	210.780(2)
130	4.00592(5)	5.15160(5)	10.35727(11)	95.015(1)	94.682(1)	97.923(1)	209.938(3)
120	3.99609(6)	5.14768(6)	10.35179(13)	95.034(1)	94.645(1)	97.965(1)	209.137(3)
110	3.98663(7)	5.14565(8)	10.34752(14)	95.080(1)	94.615(1)	97.988(1)	208.396(4)
100	3.97561(6)	5.14271(6)	10.34291(13)	95.103(1)	94.584(1)	98.029(1)	207.647(4)
90	3.96668(6)	5.13982(6)	10.33861(13)	95.127(1)	94.549(1)	98.055(1)	206.966(4)
80	3.95831(7)	5.13759(7)	10.33426(14)	95.151(1)	94.524(1)	98.077(2)	206.340(4)
70	3.95055(7)	5.13551(7)	10.33077(15)	95.185(1)	94.497(1)	98.084(2)	205.776(4)
60	3.94358(7)	5.13377(7)	10.32737(15)	95.209(1)	94.475(1)	98.096(2)	205.267(4)
50	3.93749(7)	5.13245(7)	10.32426(16)	95.235(1)	94.454(2)	98.097(2)	204.833(4)
40	3.93245(7)	5.13146(7)	10.32203(16)	95.259(1)	94.442(1)	98.094(2)	204.484(4)
30	3.92857(7)	5.13100(7)	10.32021(17)	95.279(1)	94.432(1)	98.083(2)	204.228(4)
20	3.92649(7)	5.13043(7)	10.31895(16)	95.291(1)	94.428(1)	98.076(2)	204.074(4)
10	3.92592(5)	5.13030(5)	10.31853(11)	95.296(1)	94.425(1)	98.070(1)	204.033(3)

Table S2

Refined unit-cell parameters of ethanol hemi-ammoniate. These data are plotted in Fig. S3.

T (K)	*a* (Å)	*b* (Å)	*c* (Å)	α (°)	β (°)	γ (°)	V (Å^3)
175	5.49172(1)	7.11096(2)	10.06131(2)	104.3802(2)	100.2283(2)	96.1623(2)	369.793(1)
170	5.48859(3)	7.10297(5)	10.04815(6)	104.4630(5)	100.0948(4)	96.2331(6)	368.644(3)
160	5.48197(3)	7.09051(5)	10.02501(6)	104.6053(5)	99.8834(5)	96.3358(6)	366.628(3)
150	5.47517(4)	7.08034(6)	10.00558(8)	104.712(1)	99.729(1)	96.400(1)	364.882(3)
140	5.46864(5)	7.07179(9)	9.98880(11)	104.799(1)	99.616(1)	96.444(1)	363.342(5)
130	5.46235(5)	7.06404(8)	9.97347(10)	104.877(1)	99.521(1)	96.460(1)	361.933(4)
120	5.45655(6)	7.05704(10)	9.95943(13)	104.940(1)	99.441(1)	96.481(1)	360.647(5)
110	5.45111(6)	7.05076(10)	9.94649(14)	104.999(1)	99.372(1)	96.504(1)	359.457(6)
100	5.44610(7)	7.04468(11)	9.93329(15)	105.053(1)	99.300(1)	96.518(1)	358.320(6)
90	5.44128(7)	7.03970(12)	9.92058(17)	105.111(1)	99.230(1)	96.541(2)	357.250(7)
80	5.43729(8)	7.03461(13)	9.90727(18)	105.165(1)	99.156(1)	96.555(2)	356.230(7)
70	5.43361(13)	7.03045(20)	9.89395(26)	105.215(2)	99.088(2)	96.568(3)	355.28(1)

Table S3

Parameters obtained from fitting a 2nd order Debye model to the unit-cell edges (*a*, *b*, *c*) and the unit-cell volume of ethanol mono-ammoniate, and fitting of modified polynomials to the inter-axial angles (α, β, γ). The polynomial functions are of the form, $a(T) = a_0 + a_2T^2 + a_3T^3 + a_4T^4 + a_5T^5 + a_6T^6$. The results are plotted as solid lines in Figure S2.

Debye	*a*-axis	*b*-axis	*c*-axis	Volume
V_0 (Å, Å$_3$)	3.9257(16)	5.1305(6)	10.3189(8)	204.034(13)
θ_D (K)	149(11)	236(21)	186(13)	165(4)
K_0/γ (GPa)	29(1)	48(5)	6.7(5)	17.2(3)
K_0'	7.8(8)	37(6)	9.9(5)	14.9(6)
Polynomial	α	β	γ	
a_0	95.294(3)	94.425(1)	98.063(3)	
a_2	0	0	$5.3(5)\times10^{-5}$	
a_3	$-9.3(8)\times10^{-7}$	$3.7(1)\times10^{-7}$	$-1.1(1)\times10^{-6}$	
a_4	$1.3(2)\times10^{-9}$	$-2.9(1)\times10^{-9}$	$6.4(8)\times10^{-9}$	
a_5	$-6.6(12)\times10^{-11}$	$7.1(5)\times10^{-12}$	$-1.5(2)\times10^{-11}$	
a_6	$1.2(3)\times10^{-14}$	0	0	

Table S4

Refined unit-cell parameters of deutero-ammonia. These data are plotted in the main text, Figure 12.

T (K)	*a* (Å)
180	5.13559(2)
170	5.12765(3)
160	5.11984(3)
150	5.11272(3)
140	5.10591(3)
130	5.0997(2)
120	5.0936(2)
110	5.0881(2)
100	5.0829(2)
90	5.0781(2)
80	5.0739(2)
70	5.0699(2)
60	5.0667(2)
50	5.0639(2)
40	5.0617(2)
30	5.0603(2)
20	5.0596(2)
10	5.0593(2)

Table S5

Comparison of the experimental low-temperature unit-cell parameters of ethanol mono- and hemi-ammoniate with those found at zero pressure and temperature by DFT calculation.

	Ethanol mono-ammoniate			Ethanol hemi-ammoniate		
	Expt. 10 K	DFT 0 K	Δ (%)	Expt. 70 K	DFT 0 K	Δ (%)
a (Å)	3.92592(5)	3.944321	0.469	5.4336(1)	5.310610	−2.264
b (Å)	5.13030(5)	5.031089	−1.934	7.0305(2)	6.875528	−2.204
c (Å)	10.3185(1)	10.26296	−0.539	9.8940(3)	9.918167	0.248
α (°)	95.296(1)	96.10376	0.848	105.215(2)	105.04375	−0.163
β (°)	94.425(1)	94.49019	0.069	99.088(2)	99.02780	−0.061
γ (°)	98.070(1)	94.87766	−3.255	96.568(3)	97.17857	0.632
V (Å^3)	204.033(3)	200.98713	−1.493	355.28(1)	340.14873	−4.258
b/*a*	1.30678(2)	1.27553	−2.391	1.29388(5)	1.29468	0.061
c/*a*	2.62831(5)	2.60196	−1.002	1.82088(6)	1.86761	2.566

Table S6

Parameters obtained from fitting of a 4th order logarithmic equation of state to the $E(V)$ curves of ethanol mono- and hemi-ammoniates in both their molecular and ionic forms. See main text for details of the fitted equations and Figure 14 for a plot of the curves. Since the ionic mono-ammoniate could not be relaxed below 2 GPa, the shape of the $E(V)$ curve around V_0 is not constrained and consequently the uncertainty in the fit parameters is poor. Furthermore, the value of K_0'' had to be fixed and a choice was made to use the same value found in the molecular phase.

	Ethanol mono-ammoniate		Ethanol hemi-ammoniate	
	Molecular $C_2H_5OH{\cdot}NH_3$	Ionic $C_2H_5O^-{\cdot}NH_4^+$	Molecular $2(C_2H_5OH){\cdot}NH_3$	Partially ionic $C_2H_5OH{\cdot}\ C_2H_5O^-{\cdot}NH_4^+$
V_0 (Å^3)	197.98(16)	181.8(14)	334.90(22)	319.86(10)
K_0 (GPa)	10.8(1)	15.4(12)	11.9(2)	14.00(6)
K_0'	5.9(4)	6.1(1)	7.6(2)	8.8(1)
K_0'' (GPa^{-1})	−1.1(7)	−1.1 *	−3.6(7)	−4.3(2)
E_0 (eV)	−2328.5126(6)	−2328.24(1)	−4016.5736(7)	−4016.6033(7)

*Fixed at same value as in molecular EMA.